

Technische Universität München

# Electric Field Strength and Stability Measurement Using the Linear Electro-Optic Effect in Quartz

von  
Christian Velten

## Masterarbeit in Physik

vorgelegt der  
Fakultät für Physik  
der Technischen Universität München  
im Oktober 2015

angefertigt am  
**Excellence Cluster Universe**  
Grundlagenphysik mit Neutronen  
bei  
**Prof. Dr. Peter Fierlinger**



*Primary Reviewer (PI)*

**Prof. Dr. Peter Fierlinger**  
Physics Department E18, TU München  
Excellence Cluster Universe

*Secondary Reviewer*

**Prof. Shawn Bishop, Ph. D.**  
Physics Department E12, TU München  
Nuclear Astrophysics

*Supervisor*

**Michael Sturm, M. Sc. TUM**  
Physics Department E18, TU München  
Excellence Cluster Universe



---

## Abstract

The search for permanent electric dipole moments (EDMs) of elementary particles and nucleons is driven by their ability to act as highly sensitive probes for **CP** and **T** violation and to search for physics beyond the standard model. One of those is the neutron electric dipole moment (nEDM) which several experiments worldwide search for. The current constraints put on its value already excluded some extensions to the standard model and the projected improvements will test several other theories. A next-generation nEDM experiment is being set up at the research reactor FRM-II in Garching which uses Ramsey's cycle of separated oscillatory fields and stored ultra-cold neutrons (UCNs).

One of the experiment's key features is the high voltage, applied to alter the precession frequencies of the stored neutrons due to a possible interaction with a permanent electric dipole moment. Thus, knowledge of the field and its stability during the measurement is necessary for a precise prediction of the value of or constraints on the nEDM. Within this work an optical setup capable of measuring electric fields and especially changes to it was assembled. The linear electro-optic effect in quartz, which introduces field dependent birefringence in a suitable crystal, is used for detection of electric fields. For laser stabilization a temperature-stabilized dichroic atomic vapor laser lock (DAVLL) system was integrated into the beam path. Additionally, several polarimeter boards used for laser light detection were assembled in different configurations.

The measurements were performed using a 100 mm long quartz cylinder as Pockels crystal and a power supply delivering up to  $\pm 10 \text{ kV}$ . Both, oscillating fields and sudden changes in high voltage were detected. Using a linear model the measured amplitudes were successfully matched to the expectation values. To aid analysis of the data a segmented discrete fourier transform algorithm and a software lock-in amplifier were programmed.

The results show that it is possible to measure changes in the electric field in both the frequency and time domain. However, the resolution of such measurements is highly impaired by unavoidable noise sources at the location of the setup and mechanical stabilization difficulties. Subsequently changes in the time domain were only identifiable at steps of  $2 \text{ kV}$  corresponding to a performance of  $10^{-2}$  for an envisioned field of  $1.8 \text{ kV/mm}$ . This leaves two orders of magnitudes to be achieved in further works.



---

# Contents

<b>Abstract</b>	<b>v</b>
<b>Index</b>	<b>ix</b>
<b>1. Introduction – CPT invariance and the neutron EDM</b>	<b>1</b>
<b>2. The neutron EDM, electric field systematics and the Pockels effect in quartz</b>	<b>5</b>
2.1. Measuring the neutron electric dipole moment . . . . .	5
2.1.1. The neutron electric dipole moment . . . . .	5
2.1.2. Geometric phases and motional fields . . . . .	6
2.1.3. Additional systematic effects . . . . .	8
2.2. The linear electro-optic Pockels effect . . . . .	9
2.2.1. Optical activity and polarization evolution . . . . .	11
<b>3. Experimental setup</b>	<b>15</b>
3.1. Optical setup and beam path . . . . .	15
3.1.1. Distributed feedback laser . . . . .	15
3.2. Polarimeter board . . . . .	17
3.2.1. Noise measurement . . . . .	17
3.2.2. Battery power supply . . . . .	19
3.3. Dichroic Atomic Vapor Laser Lock (DAVLL) . . . . .	20
3.3.1. Functional principle . . . . .	22
3.3.2. Assembling the DAVLL . . . . .	24
3.3.3. LDC and PID parameter tuning . . . . .	26
3.3.4. Thermal stabilization . . . . .	28
3.4. High voltage electrodes and shielding . . . . .	29
<b>4. Software development</b>	<b>33</b>
4.1. Segmented discrete Fourier transform analysis . . . . .	33
4.2. Software lock-in amplifier . . . . .	35
<b>5. Measuring the electric field induced Pockels effect</b>	<b>39</b>
5.1. Oscillating electric fields . . . . .	40
5.1.1. Background signals in the frequency domain . . . . .	40
5.1.2. Frequency transfer - capacitance limited maximum field . . . . .	41
5.1.3. Amplitude calculation . . . . .	42
5.2. Measuring absolute field values . . . . .	43
5.2.1. Semi-static electric field changes . . . . .	44
<b>6. Test operation of 200 kV high voltage supply</b>	<b>47</b>

<b>7. Conclusion and outlook</b>	<b>49</b>
<b>Bibliography</b>	<b>53</b>
<b>List of Figures</b>	<b>57</b>
<b>List of Tables</b>	<b>59</b>
<b>A. Derivations of formulas</b>	<b>III</b>
A.1. Time-dependent magnetic field . . . . .	III
A.2. Larmor precession adjustment for disturbances of an uniaxial field . . . . .	VI
<b>B. Additional figures</b>	<b>VII</b>
<b>C. Additional tables</b>	<b>XVII</b>
C.1. List of optical elements . . . . .	XVII
C.2. Cables and wiring . . . . .	XIX
C.3. Data and file formats . . . . .	XX

---

## Index

- ABS** acrylonitrile butadiene styrene  
**CC** continuous current  
**CGP** central grounding point  
**CT** constant temperature  
**CW** continuous wave  
**DAVLL** dichroic atomic vapor laser lock  
**DFB** distributed feedback laser  
**DFT** discrete fourier transform  
**EDM** electric dipole moment  
**ENBW** effective noise bandwith  
**FFT** fast fourier transform  
**FFTW** Fastest Fourier Transform in the West  
**GP** geometric phase  
**ILL** Institut Laue-Langevin  
**LD** laser diode  
**LDC** laser diode controller  
**LS** linear spectrum  
**LSD** linear spectral density  
**MAD** mean average deviation  
**MOSFET** metal–oxide–semiconductor field-effect transistor  
**ND** neutral density  
**nEDM** neutron electric dipole moment  
**NENBW** normalized equivalent noise bandwith  
**NIR** near-infrared  
**PWM** pulse width modulation  
**RBS** Ramsey-Bloch-Siegert  
**SM** Standard Model  
**SRS** Stanford Research Systems  
**TC** temperature control  
**TEC** thermoelectric cooling  
**UCN** ultra-cold neutron  
**WMAP** Wilkinson Microwave Anisotropy Probe



# CHAPTER 1

---

## Introduction – CPT invariance and the neutron EDM

The predominance of matter over antimatter is evident simply by the existence of ourselves and the world around us. The claim that we are living in a matter-dominated universe is supported using data collected by WMAP that indicates an excess baryon to photon ratio of about  $6 \times 10^{-10}$  [1, 2]. After cosmic inflation the quark-gluon plasma was made up from equal portions of particles and antiparticles, which were continuously being destroyed and created. Thus, today's predominance of baryons over anti-baryons is a strong indicator that at some point in time the symmetry between creation and destruction of particles and their counterparts was broken.

In general, physical processes are the same whether they occur mirrored, with particles replaced by the corresponding antiparticles or backwards in time. These three symmetries are known as parity (**P**), charge (**C**) and time reversal (**T**) symmetries. Thus, under **C**-, **P**- or **T**-transformation a process should exhibit the same properties. However, we know today that symmetry violating interactions exist, the most famous one being the weak interaction violating parity maximally. This was proposed in the mid-1950s and proven by the Wu-experiment in 1956 leading to the 1957's Nobel Prize in physics [3]. Also, combined symmetries of the aforementioned can be formed, for example **CP** symmetry. Violation of this symmetry was found studying the decay of  $K^0$  mesons. Until now the combined **CPT** symmetry is known to be invariant, thus any violation of **CP** is equivalent with **T** symmetry violation and vice-versa.

The discovery of those symmetry violations led to three necessary conditions, known as Sakharov criteria, to explain the observed anti-symmetry between matter and antimatter [2, 4]. Violation of baryon number conservation, **C** and **CP** symmetry violation and interactions out of thermal equilibrium. However, the sources of those symmetry violations included in the Standard Model (SM) would only lead to an excess baryon to photon ratio of  $10^{-18}$  [5] while the observation predicts a value about seven orders of magnitude higher. Thus, additional **C** and **CP** violating processes must exist. For example, a non-zero neutron electric dipole moment (nEDM), being a contribution from **CP** violating terms in the QCD's Lagrangian, would be a major contribution.

### Neutron electric dipole moment as a probe for CP violation

In contrast to classical electric dipole moments (EDMs), which are invariant under **CP** transformations, a (elementary-)particle EDM violates **T** and thus **CP** symmetry [6]. In its most common form the dipole vector is proportional to the particles' spin,  $\vec{d} = d \frac{\vec{S}}{|\vec{S}|}$  where  $d$  is a scalar and  $\vec{S}$  a pseudovector [7]. Under parity and time reversal

transformation the constituents of  $\vec{d}$  transform differently, namely

$$\begin{aligned} P(d) &= -1 & T(d) &= +1 \\ P(\vec{S}) &= +1 & T(\vec{S}) &= -1 . \end{aligned}$$

Furthermore, the value of a measured nEDM, but also constraints on its maximal value are a highly sensitive probe for the exclusion of theories extending the SM. While the value predicted in the SM is on the order of  $10^{-32}$  ecm [8] other theories, e.g. SUSY, predict higher nEDM values as they postulate more channels and interactions leading to the creation of such a property. The predictions range from  $10^{-23}$  ecm to  $10^{-29}$  ecm with the upper limit of the nEDM put at  $< 3 \times 10^{-26}$  ecm by an experiment performed at the Institut Laue-Langevin (ILL) [9]. Thus it is already possible to disprove some theoretical models as the threshold gets pushed to even lower values.

A new series of experiments aims on lowering this threshold even further by at least a factor of 100 – among them the TUM-nEDM experiment [7]. As most other experiments it utilizes Ramsey's method of separated oscillatory fields [10]. The experimental setup is similar to the experiment at the ILL [9]. However, the TUM-nEDM experiment uses two vertically aligned chambers to store ultra-cold neutrons (UCNs). A homogeneous magnetic field, the so-called  $B_0$  field, is superimposed on those chambers, which are divided by a high voltage electrode creating two separate measurement states. One with parallel and one with anti-parallel fields [11]. The Hamiltonian for this experiment and one chamber is

$$H = -\vec{\mu}_n \cdot \vec{B} - \vec{d}_n \cdot \vec{E} \equiv \hbar\omega ,$$

which is proportional to the neutron's precession frequency. Comparing the frequencies from both chambers, which can be done very precisely, leads to a measure proportional to the electric-dipole moment as the magnetic field contribution cancels out under ideal conditions,

$$d_{n,ideal} = \frac{\hbar \Delta\omega}{4E} \propto \frac{1}{E} .$$

What remains is a dependency on the electric field applied between the high voltage and the two ground electrodes. Thus, knowledge of the electric field and especially its stability over the course of one and repeated measurements is crucial as it contributes to the accuracy of each measurement.

## Optical measurement of the electric-field

Amongst the effects linked to the electric field are first, any movement of the UCNs in the electric field corresponds to a magnetic field experienced by the neutron, effectively altering the superimposed  $B_0$ -field leading to a buildup of a so-called geometric phase. Second, direct and alternating currents on the electrodes' surfaces because of

---

an unstable electric field induce magnetic fields, which alter the magnetic moment's equation of motion. And third, high voltage breakdowns lead to a high short-term magnetic field inside the neutron chamber and can also alter the magnetic profile of the components involved.

To reduce any disturbing magnetic influences the experiment set up at the research reactor FRM-II is using active and passive shielding reducing the residual field to a value lower than 1 nT [12]. Thus, it is not desirable to bring any hardware or device into the shielded area and especially near the neutron chambers that has the possibility of introducing magnetic dipoles and fields. This motivates using optical components and materials already used for the construction of the chamber to build an apparatus for electric field measurements.

The purpose of this work is to build an experimental setup for optical electric-field measurements using existing knowledge from laser-based cesium magnetometry [13]. The effect envisioned to use for field detection is the linear electro-optic effect, also known as Pockels effect, which induces birefringence proportional to the electric field in addition to natural birefringence. This should make it possible to track changes in the electric field over the course of a measurement being sensitive to field drifts and high voltage breakdowns. Using Fourier transformations to analyze portions of the recorded time series it should be possible to detect oscillating fields too small to track in the time domain. In addition to spectral analysis the concept of either hardware or software lock-ins can aid separating and extracting signals of specific frequencies from the raw data. The goal set for high voltage resolution in the TUM-nEDM experiment is set to  $10^{-4}$  of  $18 \text{ kV cm}^{-1}$  [11, 7].

The material chosen as the active component is quartz. A crystal made from  $\alpha$ -quartz was chosen as it can easily be introduced into the quartz ring which serves as the lateral surface for the neutron chambers. This way the distortion to the electric field due to change in the materials permittivity is minimized and no material made up from possibly magnetic components is used. However, quartz has one of the lowest linear electro-optic coefficients, posing a major obstacle to a high-resolution measurement.



## CHAPTER 2

---

# The neutron EDM, electric field systematics and the Pockels effect in quartz

The first part of this chapter outlines the measurement principle for a neutron electric dipole moment (nEDM) as performed in the TUM-nEDM experiment. In addition, relevant systematic effects possibly contributing to a false EDM arising from the high voltage are discussed. Detailed information on the measurement of the nEDM, design of the TUM-nEDM experiment and geometric phases can be found in Altarev et al. (2012) [11], Pendlebury et al. (2004) [14] and Golub et al. (1991) [15]. In the second part the linear electro-optic effect, also known as Pockels effect is introduced. The general formalism is used to calculate the specific behavior of quartz used in this thesis.

### 2.1. Measuring the neutron electric dipole moment

The following section outlines how a nEDM would affect the Larmor precession frequency of the neutron and deals with systematic uncertainties linked to the electric field and high voltage electrodes that generate a false EDM signal. The content of this section and especially the notation used is based on the paper by Pendlebury et al. (2004) [14].

#### 2.1.1. The neutron electric dipole moment

The Hamiltonian for a neutron in an external magnetic and electric field reads

$$H = -\vec{\mu}_n \cdot \vec{B} - \vec{d}_n \cdot \vec{E} \equiv \hbar\omega ,$$

where  $\vec{\mu}_n = \mu_n \frac{\vec{S}}{|\vec{S}|}$  and  $\vec{d}_n = d_n \frac{\vec{S}}{|\vec{S}|}$  are the neutron's magnetic and electric dipole moment, respectively. The norm of  $\vec{S}$  is  $\hbar/2$  in case of the neutron. Here  $\omega$  can be identified as  $\omega_L + \omega_E$ , which is the (standard) Larmor precession frequency of the neutron plus an electric dipole moment contribution in case of a non-zero EDM. Analogous to the Larmor frequency  $\omega_E$  is given by  $|\omega_E| = 2 d_n E / \hbar$ . By carrying out measurements with both, the electric field parallel and anti-parallel with respect to the magnetic field orientation, we receive different  $\omega$ , namely  $\omega_{\uparrow\downarrow}$  and  $\omega_{\uparrow\uparrow}$ . A common technique to measure these frequencies is Ramsey's method of separated oscillatory fields [10, 15]. The TUM-nEDM experiment is designed to use this method with two vertically aligned neutron chambers with a high voltage electrode in between and ground electrodes

on the top and bottom. This makes it possible to measure parallel and anti-parallel aligned fields at the same time, thus eliminating drifts over time of the  $B_0$  field leaving only gradients of the magnetic field affecting the measurement [11]. In this case the difference between the two frequencies for parallel and anti-parallel measurements multiplied by the measurement time  $T$  becomes

$$\begin{aligned} \hbar (\omega_{\uparrow\downarrow} - \omega_{\uparrow\uparrow}) T &= -2 \mu_n (B_{\uparrow\downarrow} - B_{\uparrow\uparrow}) T + 2 d_n (E_{\uparrow\downarrow} + E_{\uparrow\uparrow}) T + \hbar (\varepsilon_{\text{geo.}\uparrow\downarrow} - \varepsilon_{\text{geo.}\uparrow\uparrow}) \\ &\longrightarrow 4 d_n E T + \hbar (\varepsilon_{\text{geo.}\uparrow\downarrow} - \varepsilon_{\text{geo.}\uparrow\uparrow}) , \end{aligned}$$

assuming that  $\vec{\mu}_n \cdot \vec{B}_i = 2 \mu_n B_i$ , likewise for the electric field. The  $\varepsilon_i$  represent any additional phase shift accumulated in both chambers. Now,  $\Delta\phi := (\omega_{\uparrow\downarrow} - \omega_{\uparrow\uparrow}) T$  corresponds to a phase shift between the two chambers. This phase shift is measured by performing two experiments with Ramsey's method of separated oscillating fields at the same time in both chambers. From a measurement of this phase one can calculate the neutron electric dipole moment

$$d_n = \frac{\hbar \Delta\phi}{4 E T} + \frac{\hbar \Delta\omega_{\text{geo.}}}{2 E} ,$$

with  $\Delta\omega_{\text{geo.}} = -(\varepsilon_{\text{geo.}\uparrow\downarrow} - \varepsilon_{\text{geo.}\uparrow\uparrow}) T^{-1}$  being the accumulation rate for the geometric phase (GP)  $\Delta\varepsilon_{\text{geo.}}$ . The first term describes the contribution from a non-zero and stationary nEDM while the second term arises from geometric phases and is called a false EDM. The statistical accuracy with which we measure the nEDM is given by

$$\sigma_{d_n} = \frac{\hbar}{2 \alpha E T \sqrt{N} \sqrt{M}} ,$$

where  $N$  is the number of detected neutrons,  $M$  the number of measurements performed with free precession time  $T$  in an electric field of strength  $E$  including a quality parameter  $\alpha$  [11].

### 2.1.2. Geometric phases and motional fields

Neutrons traveling through electric fields experience an effective magnetic field due to the relativistic coupling of both fields,

$$\vec{B}_v = \frac{1}{c^2} \vec{E} \times \vec{v} ,$$

with which they will interact via their magnetic moment  $\mu_n$ . This effective field is perpendicular to the electric and magnetic field, since  $\vec{B}_0 \times \vec{E} = 0$ . We assume throughout these formulas that  $(\vec{B}_0, \vec{E}) \propto \hat{z}$ . A magnetic field gradient  $\partial B_0 / \partial z$  leads to a magnetic

field in the xy-plane due to  $\text{div } \vec{B} = 0$ . With cylindrical symmetry this field is [14],

$$\vec{B}_{0xy} = - \left( \frac{\partial B_{0z}}{\partial z} \right) \frac{\vec{r}}{2} .$$

These fields combined lead to an effective magnetic field in the xy-plane,

$$\vec{B}_{xy} = \left( \vec{B}_{0xy} + \vec{B}_v \right) .$$

Such non-stationary fields change the Larmor precession frequency by effectively changing the rotation frequency of the magnetic field in the rotating frame of the neutron [10]. This inevitably leads to the buildup of a GP, i.e. a shift of the Larmor frequency away from its original value given by Pendlebury in first order as

$$\Delta\omega = \frac{\omega_{xy}^2}{2(\omega_0 - \omega_r)} ,$$

with  $\omega_{xy} = -\gamma B_{xy}$ ,  $\omega_0 = -\gamma B_0$  and  $\omega_r$  being the frequency of rotation of  $B_{xy}$  as experienced by the neutron [14]. This shift is called Ramsey-Bloch-Siegert (RBS) shift. The numerator of this shift expands to

$$\omega_{xy}^2 / \gamma^2 = \vec{B}_{xy}^2 = \vec{B}_{0xy}^2 + \vec{B}_v^2 + 2 \vec{B}_{0xy} \cdot \vec{B}_v .$$

The first term represents the influence of a  $\vec{B}_0$  gradient without an electric field. The second term denotes a second-order shift with respect to  $\vec{v} \times \vec{E}$ , which cancels out in  $\Delta\omega_{\text{geo}}$  in case of electric field symmetry in both chambers. However, the third term does not cancel and since it is linear in the electric field its contribution will create a false EDM signal. For neutrons in orbits that get very close to the wall and lead to reflection under a very shallow angle the fields  $\vec{B}_{0xy}$  and  $\vec{B}_v$  experienced by the neutrons become practically parallel to the radius vector. Thus, the neutrons see rotating magnetic fields of  $B_{xy\pm} = B_{0r} \pm |B_v|$  exemplary for parallel  $B_0$  and electric field, the sign in  $\pm$  depends on the sense of rotation with respect to the main field [14]. These orbits are called "garland" orbits and Pendlebury et al. give an expression for the false EDM due to a GP in the adiabatic case with  $|\omega_r| < |\omega_0|$  for movement in such orbits [14]:

$$d_{n,f} = -\frac{\hbar}{4} \left( \frac{\partial B_{0R}/\partial z}{B_{0z}^2} \right) \frac{v_{xy}^2}{c^2} \left[ 1 - \left( \frac{\omega_r}{\omega_0} \right)^2 \right]^{-1} ,$$

using  $|B_v| = |v_{xy}| |\vec{E}| / c^2$  and the orbital frequency  $\omega_r = |v_{xy}| / R$  with trap radius  $R$  and neutron velocity  $v_{xy}$  in the xy-plane.

In addition to magnetic fields due to the neutron's movement in the electric field, this effect is also existent for the movement in magnetic fields, such as the main  $B_0$ -field,

$$\vec{E}_v = \vec{v} \times \vec{B}_0 .$$

However, since  $\mathcal{O}(B_0) \sim 10 \mu\text{T}$  the motional electric field's magnitude is rather small with  $\mathcal{O}(E_v) \sim 100 \mu\text{V m}^{-1}$  assuming  $\mathcal{O}(v) \sim 10 \text{ m s}^{-1}$  for the velocity of ultra-cold neutrons (UCNs). This makes this effect negligible compared to the planned main electric field of  $180 \text{ kV m}^{-1}$  [11].

### 2.1.3. Additional systematic effects

In addition to geometric phases there are certain effects linked to the electric field and the electrodes that need to be taken into account.

#### Direct and alternating currents

Currents  $\vec{j}$  are connected to magnetic fields via the Maxwellian equations and their (retarded) solutions. Thus, any current on the electrode's surface results in localized gradients for  $B_0$  and  $B_{xy}$ . The magnetic field of a current flowing radially to the center of the electrode is given by

$$\vec{B}(\vec{x}, t) = \frac{\mu_0 I}{4\pi} \sin(\omega_j t + \phi_j) \frac{y \hat{z} - z \hat{y}}{r^2} \left[ \frac{x}{\sqrt{x^2 + r^2}} - \frac{x - \bar{x}}{\sqrt{(x - \bar{x})^2 + r^2}} \right], \quad (2.1)$$

with the alternating (frequency  $\omega_j$ ) current  $I$  flowing radially along  $\hat{x}$  from  $x = \bar{x}$  into the center of the electrode,  $x = 0$ . For the derivation the formula see appendix A.1. This oscillating field's amplitude can get as high as  $10 \mu\text{T A}^{-1}$  for  $\vec{x} \approx (10, 0, 10)^\top \text{ mm}$  (see fig A.1). Equation (2.1) can be written as

$$\vec{B}(\vec{x}, t) = \vec{B}_{\text{AC}}(\vec{x}) \sin(\omega_j t + \phi_j).$$

There are various effects of such fields parallel and perpendicular to the main  $B_0$  field. First, any component parallel to the  $B_0$  field results in a global or localized change in the Larmor frequency  $\omega_L = \gamma(B_0 + B_{z,\text{add.}})$ , leading to the accumulation of a phase for some or all neutrons. A field perpendicular to the main field influences the Larmor frequency, too. However, it also makes the z-component of the neutron's magnetic moment time-dependent. The solution for a field  $\vec{B} = (B_x, 0, B_z)^\top$  is

$$\vec{\mu}(t) = \mu \frac{1}{1 + \alpha^2} \begin{pmatrix} \alpha^2 + \cos[\omega_L \sqrt{1 + \alpha^2} t] \\ \sqrt{1 + \alpha^2} \sin[\omega_L \sqrt{1 + \alpha^2} t] \\ 2\alpha \sin^2[\frac{1}{2}\omega_L \sqrt{1 + \alpha^2} t] \end{pmatrix},$$

with  $\alpha = \omega_x / \omega_L$ . For the derivation of this formula see appendix A.2.

Another effect that is induced by the electric field or rather a breakdown between the high voltage and ground electrode is localized change in magnetization in the

electrodes. This creation of field inhomogeneities also disturbs the measurement and after such breakdowns the magnetic profile has to be mapped again.

Because of these effects linked to the electric field it is necessary to monitor and measure its changes. Due to the requirement of low- to non-magnetic components it is reasonable to build an optical apparatus that will utilize the linear electro-optic effect exhibited by crystals which lack inversion symmetry.

## 2.2. The linear electro-optic Pockels effect

Optical properties of transparent media which affect the refractive indices can be described using the index ellipsoid  $\boldsymbol{\eta} = \epsilon_0 \boldsymbol{\epsilon}^{-1} = 1/\mathbf{n}^2$  and its construction [16],

$$\sum_{i,j} \eta_{ij} x_i x_j = 1 \quad \text{with } i, j = 1, 2, 3 .$$

The elements of the dielectric tensor  $\boldsymbol{\epsilon}$  and thus also of  $\mathbf{n}$  depend on the coordinate system chosen relatively to the substance's properties, e.g. its crystal structure. However, one can find a coordinate system which diagonalizes both tensors. The resulting system's axes define the principal axes and the diagonal elements of  $\mathbf{n}$  define the index of refraction along each axis.

Under the influence of an electric field the index ellipsoid changes and becomes dependent on  $\vec{E}$ . Expanding this dependence up to second order in  $\vec{E}$  this yields

$$\sum_{i,j} \left( \eta_{ij} + r_{ijk} E^k + s_{ijkl} E^k E^l \right) x_i x_j = 1 ,$$

using Einstein summation convention. The  $r_{ijk}$  and  $s_{ijkl}$  are the electro-optical tensors of third and fourth order. Their elements are called Pockels and Kerr coefficients respectively [17]. Since the Kerr effect is rather small it will be neglected leaving only the linear electro-optic effect:

$$\tilde{\boldsymbol{\eta}} = \boldsymbol{\eta}_0 + \text{InverseVoigt} \left[ \mathbf{r} \vec{E}^\top \right] ,$$

where a transformation from  $r_{ijk}$  to  $r_{mk}$  was made due to symmetry of the tensor [16]. The rules for identifying  $i, j \mapsto m$  are those of the Voigt notation. The InverseVoigt operation is defined as

$$\text{InverseVoigt} \left[ (a, b, c, d, e, f)^\top \right] := \begin{pmatrix} a & f & e \\ f & b & d \\ e & d & c \end{pmatrix} .$$

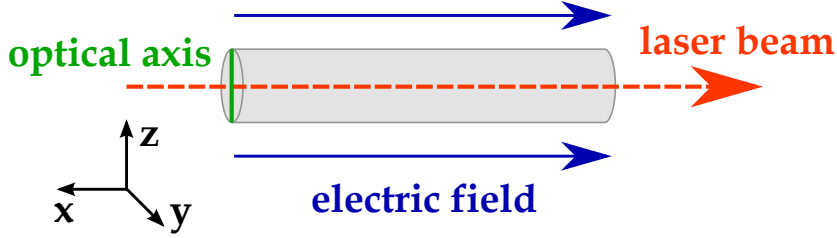


**Figure 2.1.:** Sketch of quartz crystal with alignment of the optical axis, laser beam and electric field. Both, the field and laser beam are parallel to the cylinder axis while the optical axis is perpendicular to it.

To diagonalize one has to calculate the eigenvalues and eigenvectors of  $\tilde{\eta}$ ,

$$\det(\tilde{\eta} - \lambda \mathbf{1}) \stackrel{!}{=} 0 .$$

### Pockels effect in quartz with defined electric field

The only non-zero electro-optic coefficients in  $\alpha$ -quartz are in reduced form  $r_{41}$  and  $r_{11}$  with the electro-optic tensor [18],

$$\mathbf{r}^T = \begin{pmatrix} r_{11} & -r_{11} & 0 & r_{41} & 0 & 0 \\ 0 & 0 & 0 & 0 & -r_{41} & -r_{11} \\ 0 & 0 & 0 & 0 & 0 & 0 \end{pmatrix} .$$

The setup designed in this thesis includes a quartz crystal in cylindrical shape, with its optical axis perpendicular to the cylinder axis. Both, the laser beam and the electric field are aligned parallel to the cylinder axis. For reference, see figure 2.1.

Assuming an electric field in x-direction,  $\vec{E} = (E, 0, 0)^T$ , the eigenvalue problem,

$$\begin{vmatrix} (\eta_1 + r_{11} E) - \lambda & 0 & 0 \\ 0 & (\eta_2 - r_{11} E) - \lambda & r_{41} E \\ 0 & r_{41} E & \eta_3 - \lambda \end{vmatrix} \stackrel{!}{=} 0 ,$$

is easily solvable. The result is a diagonal matrix  $\Lambda = S^{-1} \tilde{\eta} S = \text{diag}(\lambda_1, \lambda_2, \lambda_3)$  with

$$\begin{aligned} \lambda_1 &= \eta_1 + r_{11} E \\ \lambda_{2,3} &= \frac{1}{2} \left[ \eta_2 + \eta_3 + r_{11} E \mp \sqrt{(2r_{41} E)^2 + (\eta_2 - \eta_3 + r_{11} E)^2} \right] . \end{aligned}$$

This leads to the new refractive indices ( $n_i = \lambda_i^{-1/2}$ ), expanded to the first significant

order in  $E$ ,

$$\begin{aligned} n'_1 &= n_1 \left( 1 - \frac{1}{2} r_{11} n_1^2 E + \mathcal{O}[E^2] \right) \\ n'_2 &= n_2 \left( 1 - \frac{1}{2} r_{11} n_2^2 E + \mathcal{O}[E^2] \right) \\ n'_3 &= n_3 \left( 1 + \frac{1}{2} r_{41}^2 \frac{n_2^2 n_3^4}{n_3^2 - n_2^2} E^2 + \mathcal{O}[E^3] \right). \end{aligned}$$

The quadratic term in  $n'_3$  is negligible due to the small value of  $r_{41}^2$ . Thus, two of the refractive indices are changed in terms of the linear electro-optic effect in quartz. The one unchanged refractive index is the one for directions parallel to the optical axis.

### 2.2.1. Optical activity and polarization evolution

Quartz is a birefringent material with  $\Delta n^{(0)} = n_3 - n_2 \approx -0.0887$  at 850 nm [19]. The electro-optic effects change this normal birefringence depending on the electric field leading to

$$\Delta n = \Delta n^{(0)} + \Delta n^{(E)} = \Delta n^{(0)} + \frac{1}{2} r_{11} n_2^3 E .$$

The difference in refractive indices for different polarization states results in the retardation of one of the components compared to the other. Over a distance  $l$  this leads to an accumulation of a phase difference

$$\Delta\phi = \frac{2\pi}{\lambda_0} \Delta n l = \Delta\phi^{(0)} + \frac{\pi}{\lambda_0} r_{11} n_2^3 E l , \quad (2.2)$$

where  $\lambda_0$  is the wavelength outside the crystal.

### Jones calculus for light polarization

When light propagates through free space it can be described as transverse waves of electric and magnetic fields, which are orthogonal to the direction of propagation. Thus, the electric field vector  $\vec{E}$  can be reduced to a two-dimensional vector

$$\vec{E} = (E_{0x} e^{i\phi_x}, E_{0y} e^{i\phi_y})^\top \cdot e^{i(kz - \omega t)},$$

where the first part holding the amplitude and phase information is the so called *Jones vector* [20]. Two examples for linear polarized light, first in  $x$ -direction and second with a  $45^\circ$  angle between both the  $x$ - and  $y$ -axis, are (normalized)

$$\begin{pmatrix} 1 \\ 0 \end{pmatrix} \text{ and } \frac{1}{\sqrt{2}} \begin{pmatrix} 1 \\ 1 \end{pmatrix} .$$

Optical elements and their influence on the light are described by the *Jones matrices* with a linear polarizer and a retarder being represented by [20]

$$\mathcal{A}_{\text{pol}}(0) = \begin{pmatrix} 1 & 0 \\ 0 & 0 \end{pmatrix} \text{ and } \mathcal{A}_{\text{ret}}(\phi_x, \phi_y) = \begin{pmatrix} e^{i\phi_x} & 0 \\ 0 & e^{i\phi_y} \end{pmatrix} .$$

However, since the polarization of the light beam gets defined by a rotating linear polarizer (see sec. 3.1) the polarization direction will likely be neither parallel nor perpendicular to the Pockels crystal's optical axis. For simplicity reasons the direction set by the polarizer shall be  $(1, 0)^T$ . The Jones matrix corresponding to the retardation in the Pockels crystal is then given by

$$\tilde{\mathcal{A}}_{\text{ret}} = \mathbf{R}(\vartheta) \mathcal{A}_{\text{ret}} \mathbf{R}^T(\vartheta) = \begin{pmatrix} e^{i\phi_x} \cos^2 \vartheta + e^{i\phi_y} \sin^2 \vartheta & (e^{i\phi_x} - e^{i\phi_y}) \cos \vartheta \sin \vartheta \\ (e^{i\phi_x} - e^{i\phi_y}) \cos \vartheta \sin \vartheta & e^{i\phi_y} \cos^2 \vartheta + e^{i\phi_x} \sin^2 \vartheta \end{pmatrix} ,$$

with the rotation matrix  $\mathbf{R}(\vartheta) = \begin{pmatrix} \cos \vartheta & -\sin \vartheta \\ \sin \vartheta & \cos \vartheta \end{pmatrix}$  and  $\vartheta$  as the angle between the optical axis and direction of polarization. The matrix  $\mathcal{A}_{\text{ret}}$  contains the retardation imposed by natural and Pockels effect induced birefringence. The beam is split into two perpendicular polarized beams using a Wollaston prism. Since the prism's axes of discrimination are also rotated (angle  $\gamma$ ) with respect to the polarization set by the polarizer, one has to rotate the Jones vector before both amplitudes can be easily extracted from it. With  $\psi_{\text{in}} = (1, 0)^T$  the final vector is

$$\begin{aligned} \psi_{\text{fi}} &= \mathbf{R}(\gamma) \mathbf{R}(\vartheta) \mathcal{A}_{\text{ret}} \mathbf{R}^T(\vartheta) \psi_{\text{in}} \\ &= \left( \begin{bmatrix} e^{i\phi_x} \cos^2 \vartheta + e^{i\phi_y} \sin^2 \vartheta \\ (e^{i\phi_x} - e^{i\phi_y}) \cos \vartheta \sin \vartheta \end{bmatrix} \cos \gamma - \begin{bmatrix} (e^{i\phi_x} - e^{i\phi_y}) \cos \vartheta \sin \vartheta \\ e^{i\phi_x} \cos^2 \vartheta + e^{i\phi_y} \sin^2 \vartheta \end{bmatrix} \sin \gamma \right) \\ &= \begin{pmatrix} e^{i\phi_x} \cos \vartheta \cos(\vartheta + \gamma) + e^{i\phi_y} \sin \vartheta \sin(\vartheta + \gamma) \\ e^{i\phi_x} \cos \vartheta \sin(\vartheta + \gamma) - e^{i\phi_y} \sin \vartheta \cos(\vartheta + \gamma) \end{pmatrix} . \end{aligned}$$

Both components can be further simplified to yield the relative intensities

$$\begin{aligned} |\psi_{\text{fi}\parallel}|^2 &= \frac{1 + \cos 2\vartheta \cos 2\tilde{\vartheta}}{2} + \frac{\sin 2\vartheta \sin 2\tilde{\vartheta}}{2} \cdot \cos(\phi_x - \phi_y) \\ |\psi_{\text{fi}\perp}|^2 &= \frac{1 - \cos 2\vartheta \cos 2\tilde{\vartheta}}{2} - \frac{\sin 2\vartheta \sin 2\tilde{\vartheta}}{2} \cdot \cos(\phi_x - \phi_y) , \end{aligned}$$

using  $|\psi|^2 = \psi \bar{\psi}$ , where  $\bar{\psi}$  is the complex conjugate. Additionally  $\tilde{\vartheta} = \vartheta + \gamma$  is used. Correctly, the sum of both magnitudes equals unity. The interesting quantity, the difference between both intensities is

$$|\psi_{\text{fi}\parallel}|^2 - |\psi_{\text{fi}\perp}|^2 = \cos 2\vartheta \cos 2\tilde{\vartheta} + \sin 2\vartheta \sin 2\tilde{\vartheta} \cdot \cos(\phi_x - \phi_y) .$$

The effect of the natural birefringence and Pockels effect are encoded in the phase difference  $\Delta\phi = |\phi_x - \phi_y|$ . To have an intensity difference measure in units of W, one has to multiply with the total beam intensity after the polarizing beam split-

ter,  $\Delta I = I_0 \left( |\psi_{fi\parallel}|^2 - |\psi_{fi\perp}|^2 \right)$ . The sine and cosine terms will be replaced by  $s(\vartheta, \tilde{\vartheta})$  and  $c(\vartheta, \tilde{\vartheta})$  respectively. Comparing the phase difference above with the one in equation 2.2, this leads to

$$\frac{\Delta I}{I_0} = c(\vartheta, \tilde{\vartheta}) + s(\vartheta, \tilde{\vartheta}) \cos \left( \frac{\pi r_{11} n_2^3 l}{\lambda_0} E + \Delta\phi^{(0)} \right). \quad (2.3)$$

However, most of the times the differential signal given at a certain time will be compared against a previous one. For  $\frac{\pi r_{11} n_2^3 l}{\lambda_0} E \ll \Delta\phi^{(0)}$  the above equation can be approximated to

$$\frac{\Delta I}{I_0} \approx c(\vartheta, \tilde{\vartheta}) + s(\vartheta, \tilde{\vartheta}) \left[ \cos \Delta\phi^{(0)} - \frac{\pi r_{11} n_2^3 l}{\lambda_0} E \sin \Delta\phi^{(0)} \right].$$

The difference between two signals separated in time, but acquired with the same configuration, then is

$$\Delta(A, B) := \frac{\Delta I}{I_0} \Big|_B - \frac{\Delta I}{I_0} \Big|_A = -\frac{2 \pi r_{11} n_2^3 l}{\lambda_0} s(\vartheta, \tilde{\vartheta}) \sin \Delta\phi^{(0)} \cdot (E_B - E_A). \quad (2.4)$$



# CHAPTER 3

---

## Experimental setup

The experimental setup was designed from scratch using existent knowledge from Michael Sturm and his work on laser-based Cs-atomic magnetometers [13] currently in development. Using already existent technology, components and knowledge thereof makes it easier to transfer techniques and components between experimental setups. A list of used optical parts, other than post assemblies or similar is available in the appendix (see app. C.1).

### 3.1. Optical setup and beam path

The experiment and optical components are set up on top of a breadboard. A schematic drawing of the laser beam path is shown in figure 3.1. To store all the devices needed for operation of this setup and to keep the optical breadboard clear of excess objects a special table was built. It features a storage level for devices and is made from aluminum profiles compliant with those sold by item Industrietechnik GmbH as production series 8 (see fig B.11).

The path starts with the distributed feedback laser diode followed by an aspheric lens with focus length  $f = 3.1\text{ mm}$ , which is used to focus and collimate the diode's highly divergent emission. The lens is therefore placed less than a millimeter away from the diode window. Next in line is an optical isolator, which linearly polarizes the beam to some extent and prevents light from being reflected into the laser diode. It is followed by a beam sampler to route a portion of the light into the DAVLL system.

To reduce the intensity of the laser beam, one or multiple neutral density (ND) filters can be inserted into the path at this point. The beam is then directed through a  $\lambda/2$  waveplate and a linear polarizing foil, both of which can be rotated independently. They are followed by the high voltage section consisting of a Faraday cage, electrodes and quartz crystal. After this the beam is split using a Wollaston prism, creating two orthogonal linear polarized beams to be measured by the readout polarimeter board.

#### 3.1.1. Distributed feedback laser

The laser used in this setup is an eagleyard distributed feedback laser (DFB) diode (EYP-DFB-0852-00150-1500-TOCo3-0005) operated using a Stanford Research Systems LDC501. This diode emits quasi-monochromatic laser light with small linewidth, reducing noise and fluctuations due to any wavelength dependence of optical elements

### 3. Experimental setup

---

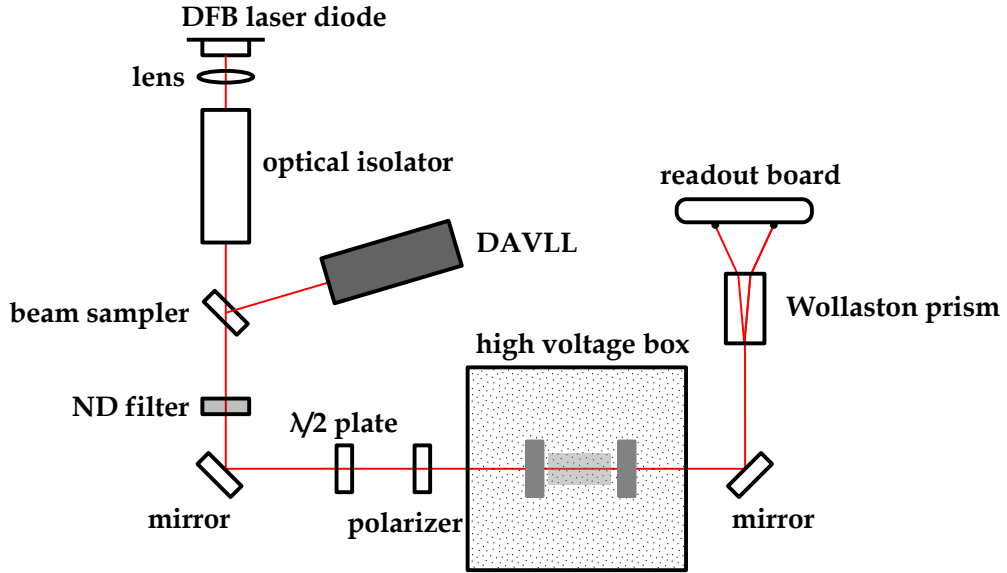


**Figure 3.1.:** Sketch of the optical setup and beam path. It starts in the top left with the laser diode and continues through the high voltage box towards the readout board. The high voltage box contains two electrodes and a quartz crystal. A part of the laser beam is extracted and fed into a dichroic atomic vapor laser lock (DAVLL) for active stabilization.

and effects. In addition, using a laser diode emitting 852 nm light allows to use a cesium-based dichroic atomic vapor laser lock (DAVLL) system. The diode's emitted wavelength is dependent on the temperature and operating current. This is due to the design of a DFB laser which uses a diffraction grating as active region, hence yielding different resonance wavelengths depending on the temperature. A change in current also leads to temperature changes inside the diode, triggering the same effect. A more detailed description of distributed feedback lasers is given by Seufert et al. (2004) [21].

The Stanford Research Systems LDC501 used to operate the laser diode is connected to the diode's TOC-3 socket using two cables for the laser diode current and thermoelectric cooling (TEC). To protect the laser diode from high voltages in the event of unplugging it, a protection circuit is soldered and installed between laser diode and cable (see fig. B.1). The wiring is shown in table C.3.

Because of the influence of diode temperature and laser current, the LDC's temperature control (TC) unit is operated in constant temperature (CT) mode at 32 °C. The operation current is coarsely set to 201.70 mA as it is also set and controlled by a feedback loop (see sec. 3.3).

## 3.2. Polarimeter board

Detecting small intensity differences with separate detectors and differential amplifiers can be a hard task to accomplish due to intrinsic noise of each component and noise pick-up between each component. Thus, an existent layout for a polarimeter board is used throughout this setup, which combines the detector and amplification stages on one circuit board [13].

Aside from two Hamamatsu S3072 photo-diodes the polarimeter board hosts two single-sided and one differential path (see fig B.2). First the photo-diodes convert incident light into currents. In case of the single-sided paths, these are passed through a current mirror to a trans-impedance amplifier, which transforms them into a voltage signal. Within the differential path the current from the photo-diodes gets subtracted from one another and converted into a voltage signal in a trans-impedance amplifier with separate specifications to those in the single-sided paths. This voltage signal is now further amplified using a normal amplifier. The last stage for all three signals is the SMA connection. To make the board DC-coupled, capacitor slot C6 is shorted.

The voltage signal relates to incident intensity via the photo-diode's spectral response and the amplification factor. The Hamamatsu S3072's average response is given as  $0.56 \text{ A W}^{-1}$  at  $830 \text{ nm}$  [22] and the amplification and conversion factor of the differential channel is  $10 \text{ mV nA}^{-1}$  yielding

$$U(I) = 5.6 \text{ V } \mu\text{W}^{-1} \cdot I .$$

In addition to the parts listed within figure B.2 there is also a modified parts list for a even lower noise configuration. This low-noise configuration is used as the polarimeter boards in the DAVLL (see sec. 3.3) and as the measurement board. A number of board with both configurations were assembled.

To record the board's output it is connected to a Tektronix oscilloscope using BNC to SMA connectors. It is connected to and controlled via USB by a Raspberry Pi.

### 3.2.1. Noise measurement

Measuring the board's noise density with both photo diodes covered is essential to assess whether the assembly and especially the soldering was performed properly. Aside from damaged components, one major effect of improper soldering is the creation of little antennas. These spikes of solder capture electromagnetic fields and increase the board's noise.

The measurement of the board's dark noise was performed using a Stanford Research Systems (SRS) SR830 lock-in amplifier with a SRS DS345 as external frequency source. The board's differential output was connected to the SR830's A input. The lock-in's parameters are shown in table 3.1.

### 3. Experimental setup

---

Parameter	Value	Command
coupling	AC	ICPL 0
gain / sensitivity	5 mV/nA, 20 mV/nA	SENS 19, SENS 21
time constant	100 ms	OFLT 8
reserve mode	Low Noise	RMOD 2
low pass filter slope	24 dB/oct	OFSL 3
display CH <sub>1,2</sub>	XNOISE,YNOISE	DDEF 1,2;DDEF 2,2
output CH <sub>1,2</sub>	display	FPOP 1,0;FP0P2,0
data sampling	512 Hz	SRAT 13
acquire mode	LOOP	SEND 1

**Table 3.1.:** Lock-in parameters for the polarimeter board's noise measurements.

Two voltage sources were used to assess their influence, a battery box currently under development in the Cs-group (sec. 3.2.2) and a block of 9 V batteries. When using the battery box, the polarimeter board was inside the box, enclosed by thin plates of aluminum and the differential signal was routed via SMA connectors on the box. In case of the 9 V batteries the board was put into a cardboard box and care was taken to straighten out the wires from the batteries as well as the cables leading to the lock-in to minimize pick-up of electromagnetic fields.

Measurements were performed using Python scripts controlling the function generator and reading the registers from the lock-in. The Stanford Research Systems SR830 stores the values that are calculated to be displayed for CH1 and CH2 in its internal register. After setting a new frequency  $f$ , the script is paused for  $1\text{s} + 2/f$  for the frequency to settle before the acquisition method is called. The terms  $1\text{s}$  and  $2/f$  are chosen for a general buffer for the electronics to settle and for twice the cycle time to make sure the reference signal is properly fed from the DS345 to the lock-in. The lock-in's data acquisition is paused, registers cleared and started again. First, we wait hundred times the time constant to acquire some data and begin the averaging process. Second, we let the lock-in calculate  $n$  more data points, which are then read from the internal registers. Subsequently mean and standard deviation are calculated for both channels ( $x$  and  $y$ ). This yields for each frequency  $f$  a noise value  $\sqrt{\langle x \rangle^2 + \langle y \rangle^2}$  and corresponding uncertainty. Noise estimation and calculation by the SR830 is performed calculating the mean average deviation (MAD) for  $X$  and  $Y$  and scaling the results using the effective noise bandwidth (ENBW) [23]. Section 4.2 deals with how  $X$  and  $Y$  are calculated by a lock-in amplifier.

The results for noise measurements with different power sources are shown in figure 3.2. Here the black data points represent a measurement for frequencies of  $10^{-1}\text{Hz}$  to  $10^5\text{Hz}$  using the 9 V battery pack. The red points show the measurement with the battery box for frequency values from 1 Hz to  $10^5\text{Hz}$ . At 60 Hz and 120 Hz the

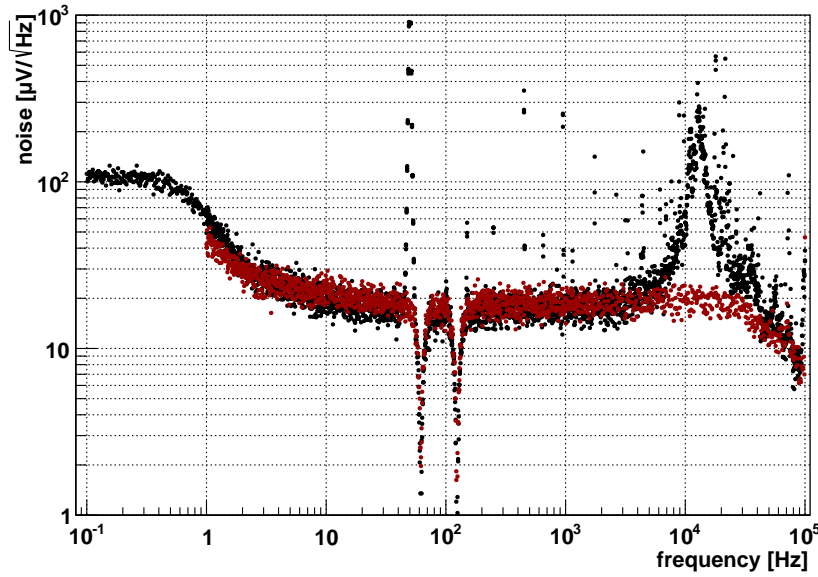


**Figure 3.2.:** Polarimeter board noise spectrum measured using a SRS lock-in amplifier. As voltage sources 9 V batteries (black) and the existing battery box (red) were used. The box also shields the board due to its closed aluminum housing.

Stanford Research Systems SR830's configuration suppresses any noise, while the instruments are operated in a 50 Hz grid. However, this peak only shows in the noise spectrum recorded with the 9V batteries pack setup where the board and batteries were placed in a cardboard box.

The measured noise floor value of roughly  $20 \mu\text{V}_{\text{rms}}/\sqrt{\text{Hz}}$  is within one order of magnitude of previous measurements by Sturm (2013) [13] with  $2.45 \mu\text{V}_{\text{rms}}/\sqrt{\text{Hz}}$ . Despite this, the measured noise floor is still acceptable.

### 3.2.2. Battery power supply

The planned Cs-magnetometer array will utilize more than sixteen separate polarimeter boards that continuously need to be supplied with power. The current power supply consists of (multiples of) two 9 V batteries, delivering  $\approx 9 \text{ V}$  and a common ground. However, replacing those batteries on an almost daily basis is both, highly inconvenient and with time costly.

At the begin of this thesis the first version of the battery power supply has already been built by the Cs-group, but it was not characterized how it would perform compared to the 9 V batteries and accomplish its designated objective: flat discharge curve, high capacity, automatically switching from one battery block to another and shielding the polarimeter boards from external fields reducing the board's noise.

The influence of the aluminum housing on the noise on the polarimeter board was measured as described above (sec 3.2.1). From the results shown in figure 3.2 it is

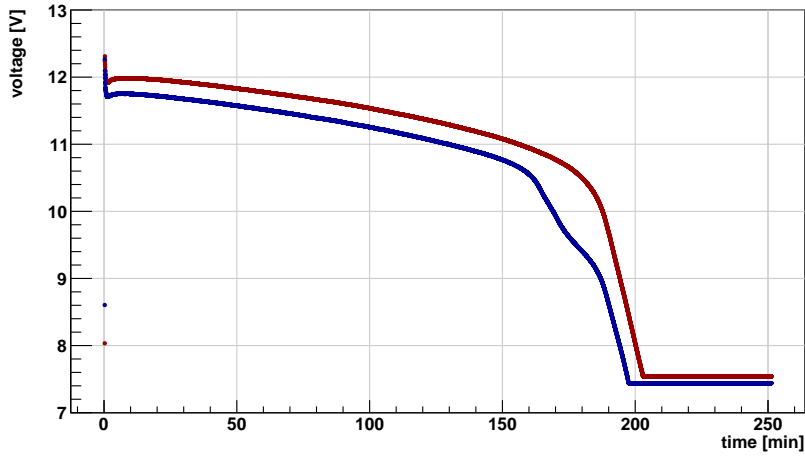


**Figure 3.3.:** Discharge curve for both polarities (+ : red, - : blue) using two 45 W lamps. After the light has been connected the voltage drops rapidly by approximately 0.5 V before it passes into a discharge curve with a lower slope.

evident that using the battery box reduces the noise at some discrete frequencies at and higher than 50 Hz. It also removes the broad peak at approximately 10 kHz to 20 kHz probably stemming from the fluorescent lamps which operate at several kHz.

However, the overall noise level is not decreased in any way. The noise shape, frequency dependence and magnitude match those from the 9 V battery measurement. Thus, the box effectively protects the board from picking up several discrete frequencies, but cannot reduce the overall noise level any further. This indicates that the measured noise floor is primarily defined by the polarimeter board and electronics.

For recording of the battery box's discharge curve, two 45 W lamps were connected via a common ground to the positive and negative terminal respectively. The voltage was measured using an oscilloscope. The discharge curve recorded using the Python script `PowerBox_Discharge.py` is shown in figure 3.3. Starting with fully charged batteries both voltages drop rapidly but recover within seconds to approximately 12 V with one battery being less charged than the other. It takes around 150 min, corresponding to 86.25 Wh, for the batteries' voltages to reduce by 1 V. At this point the voltage begins to drop faster and with different shapes and after another 50 min the voltage on both batteries is too low to run the lamps. Automatic switching between the two battery blocks and charging was not tested as it was not yet properly implemented.

### 3.3. Dichroic Atomic Vapor Laser Lock (DAVLL)

To assess the setup's stability, several hour-long measurements of the measuring board's differential and single-sided outputs were performed. At first these measure-

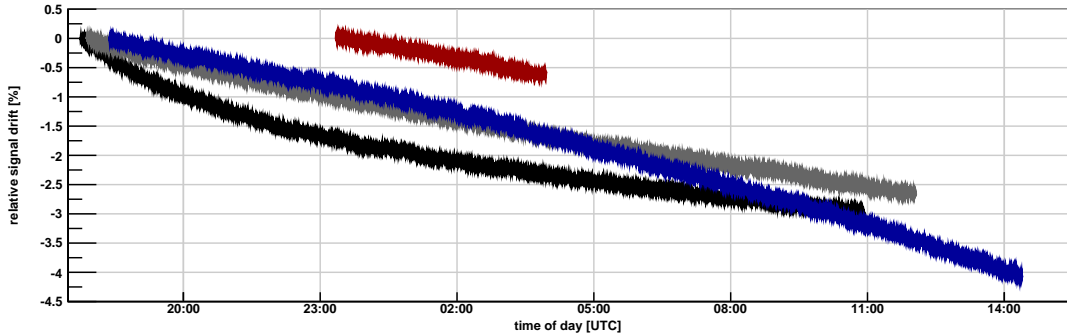


**Figure 3.4.:** Repeated measurement (different colors) of the polarimeter board's differential signal over several hours showing the drift attributed to a change in the laser light wavelength.

ments were performed with the complete beam-path, showing a repeatable signal drift (see fig. 3.4). The drift showed some correlation with the ambient temperature. However, the calculated covariance was inconsistent between measurements and the drift showed the same behavior for different measurement periods and times. Due to the  $\lambda/2$ -plate (850 nm) and the Wollaston prism the setup is highly sensitive to changes in the light's wavelength resulting in different intensities on the final polarimeter board.

Since the wavelength emitted by distributed feedback laser (DFB) diodes is directly proportional to both, the diode temperature and the laser diode current these two factors can contribute to a wavelength drift [21]. However, the laser diode temperature is set via the laser diode controller (LDC) and remains in continuous wave (CW) operation constant only changing back and forth on the order of 1 mK. It is thus reasonable to attribute the drift to a change in the laser diode's wavelength due to the laser diode's (LD) current. To further investigate the origin of the drift, the beam-path was shortened to include only the collimating lens, beam sampler, one ND-filter, a  $\lambda/2$ -plate and Wollaston crystal, thus removing any possible influences of the optical isolator, mirrors or the high voltage box. But still, the drift persisted and emphasized the need for an active laser stabilization.

As was shown by Corwin et al. (1998) [24] and Yashchuk et al. (2000) [25] a so called dichroic atomic vapor laser lock (DAVLL) can be used for active frequency and thus wavelength stabilization of laser diodes. Utilizing magnetically induced circular dichroism in atomic vapor, i.e. wavelength dependent absorption of light, a frequency error signal is produced that passes through zero at the lock frequency, providing a suitable lock signal [25]. Compared to other techniques this method remains stable for a long time and can be assembled as a small unit with few optical and electronic parts [24].

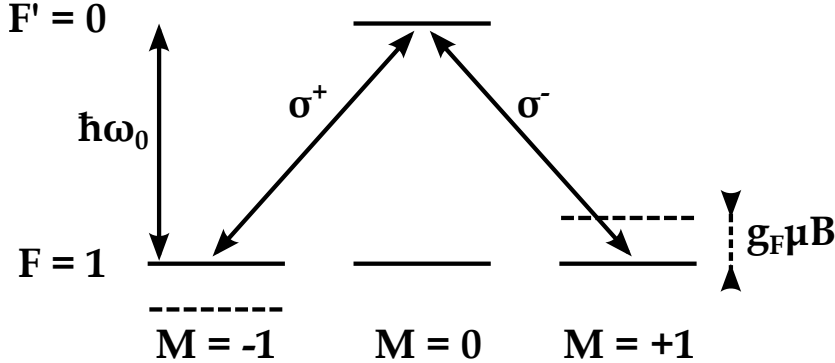


**Figure 3.5.:** Level scheme for the  $F = 1 \rightarrow F' = 0$  transition and Zeeman splitting of the ground state used for the DAVLL technique.

### 3.3.1. Functional principle

The DAVLL built for this setup utilizes two effects in cesium vapor that is exposed to a small magnetic field, Zeeman splitting of cesium's D<sub>2</sub>-line and circular dichroism of the atomic vapor. Using these effects a frequency error signal is produced and fed to a control circuit. The laser beam used in the DAVLL circuit is linearly polarized ( $\pi$ ) and can thus be described as a superposition of two circularly polarized beams ( $\sigma^+$  and  $\sigma^-$ ).

In a simple case of a transition from the ground state to an excited state with hyperfine quantum numbers  $F = 1 \rightarrow F' = 0$  the excited state is primarily populated using circularly polarized light  $\sigma^+$  and  $\sigma^-$  for  $|F; -1\rangle \rightarrow |F'; 0\rangle$  and  $|F; 1\rangle \rightarrow |F'; 0\rangle$  respectively (see fig. 3.5). In absence of an external magnetic field the ground state  $|F; M\rangle$  is degenerate with  $M = \pm 1$ , thus the absorption frequencies for both circular polarizations are the same [25]. When a magnetic field is applied the hyperfine sub-levels interact with the field [26],

$$H_B = \frac{\mu_B}{\hbar} (g_S \vec{S} + g_L \vec{L} + g_I \vec{I}) \cdot \vec{B} \equiv \frac{g_F \mu_B}{\hbar} \vec{F} \cdot \vec{B} .$$

This shifts the resonance frequency for  $\sigma^\pm$  light absorption by  $\mp g_F \mu_B B / \hbar$  to  $f_{D_2}^{(\mp)}$ . The absorption resonances are Doppler-broadened due to the movement (approximately  $240 \text{ m s}^{-1}$  at  $30^\circ\text{C}$ ) of the cesium atoms, with a typical width  $\Gamma \sim 2\pi \text{ GHz}$  [25]. These resonances describe frequencies at which the absorption of either  $\sigma^+$  or  $\sigma^-$  light is more likely to happen. Thus, between both resonances there is a value at which the absorption probability for both circular polarizations is equal. This value corresponds to a shift  $\Delta f := f - f_{D_2}^{(0)} = 0$  and also to  $S_{\text{diff.}}(0) = 0$ , with  $S_{\text{diff.}}(\Delta f)$  as the differential signal. Since the differential signal's shape changes with the temperature of the cesium cell, it is beneficial to chose  $S_{\text{diff.}}^{(0)}(0) = S_{\text{diff.}}^{(1)}(0) = 0$  as setpoint, i.e. lock frequency and signal for the feedback loop. The temperature dependence is a result of the cesium's vapor pressure changing with temperature as well as a different Doppler-broadening. This effect is qualitatively shown in figure 3.6.

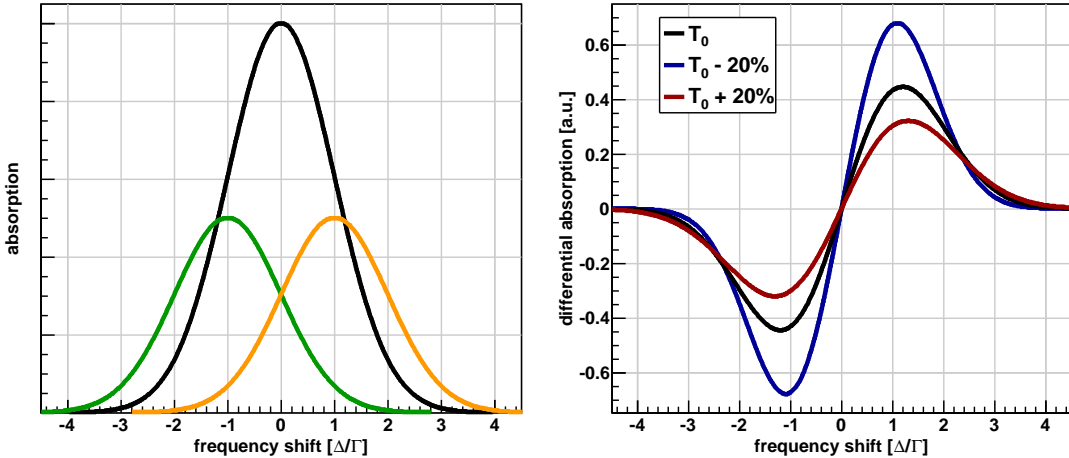


**Figure 3.6.:** Qualitative illustration of the the magnetic field influence on the absorption resonances (left) and the resulting differential signal, with  $\Delta = g_F \mu_B B / \hbar$  and the resonance width  $\Gamma$ . The absorption resonances are shifted from  $f_{D_2}^{(0)}$  (black) to  $f_{D_2}^{(\mp)}$  (green, orange) yielding a differential signal  $S_{\text{diff.}}(\Delta f)$  (right). The temperature dependence is shown for extreme changes  $T_0 \pm 20\%$  ( $T$  in Kelvin).

The DAVLL is operated as a circular analyzer as described by Corwin et al. (1998) [24]. Using a beam sampler a small fraction of the light transmitted through the optical isolator is rerouted through an absorptive ND filter with  $ND = 5$ . The beam then passes a  $\lambda/2$  wave-plate used to adjust the linear polarization's angle relative to the Wollaston prism. The angle is chosen such that the prism splits the beam into two parts with equal intensity for frequencies outside the resonances, setting the differential signal's baseline to zero. After the  $\lambda/2$  wave-plate the beam passes a glass cell filled with cesium vapor in which the two circular components of the initial  $\pi$ -polarized light are absorbed according to the Zeeman-shifted resonances. This reduces the intensity of both components differently leading to elliptically polarized light. The following  $\lambda/4$  wave-plate transforms the circular polarizations into  $\pi$ -polarizations, which superimposed again yield a linearly polarized beam. Its polarization, however, is rotated against the initial one according to the absorption of  $\sigma^\pm$  light in the Cs-cell. The linear polarization is then analyzed with a Wollaston prism as polarizing beam-splitter and a polarimeter board.

In general polarimeter boards used for DAVLL systems and signal measurements are designed differently. While readout-boards need to be fast and the DC-signal is negligible, as is the case for operation of Cs-magnetometers for example, the boards used for DAVLL systems need to be stable and resistant to noise pickup. Thus, DAVLL boards are operated DC-coupled while readout-boards are commonly assembled to operate in AC-coupled. However, the boards used in this experiment are both DC-coupled without negative implications for either applications.

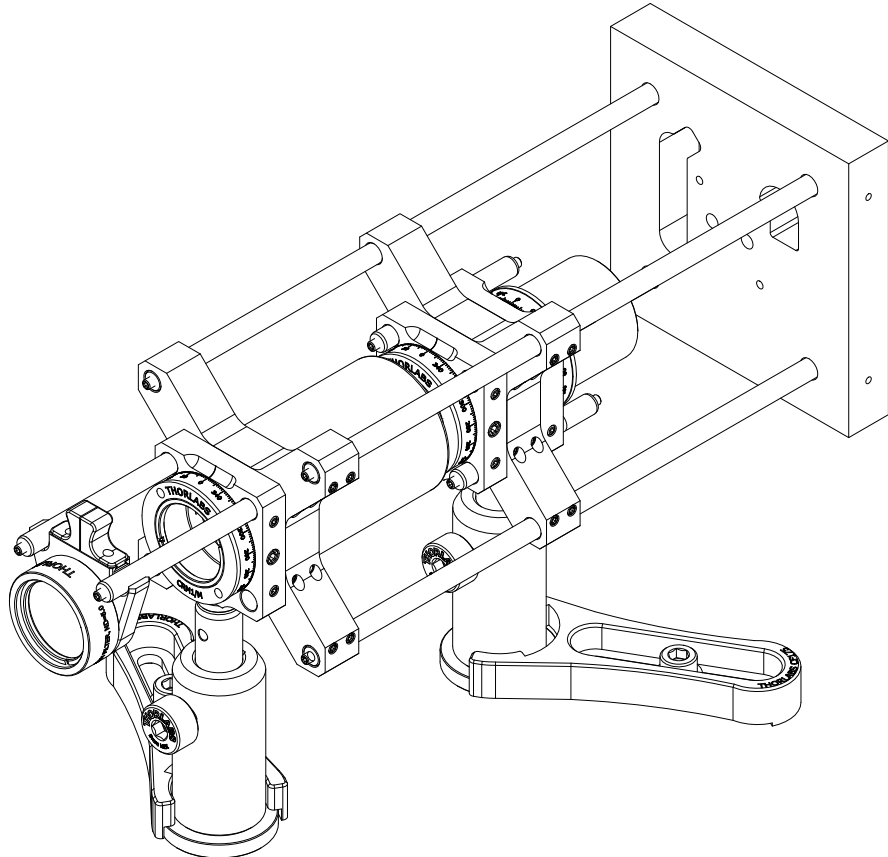


**Figure 3.7:** SolidWorks® sketch of DAVLL optical setup. The polarimeter board and temperature stabilizing cover are not shown here. The laser beam enters from the lower left.

### 3.3.2. Assembling the DAVLL

The cell used for the DAVLL operation is a glass cylinder about 30 mm long and 10 mm wide without a paraffin anti-relaxation coating. Its stem hosts cesium that is evaporated into the cell volume. The cell is surrounded by permanent magnets creating a field of 20 mT (COMSOL® simulation) [27]. To trap the field lines inside the DAVLL system the cell and magnet are shielded with Mu-metal, a metal with a very high permeability.

The optics part of the DAVLL is built into a 60 mm cage system using adapter plates for 30 mm to accommodate the mounts. The ND-filter,  $\lambda/2$  wave-plate and the DAVLL-cell are located on the front adapter plate, which separates the last two components. The  $\lambda/4$  wave-plate and the Wollaston prism follow on the rear plate. A board retainer was designed and 3D-printed to host the polarimeter board. Figure 3.7 shows a SolidWorks® drawing of the optical DAVLL setup without the polarimeter board and temperature stabilizing cover.

As described above, this setup creates two spatially separated laser beams that are

detected using a polarimeter board in low-noise configuration (see sec. 3.2). In normal operation mode only the differential output is of concern and connected. However, for debugging purposes and adjustment of the photo-diodes both single sided outputs are connected to and displayed on the oscilloscope. Coarse adjustment was performed using a laser viewing card for near-infrared (NIR) and visually extrapolating the beam path onto the detector's active area. Fine-tuning was successfully done by maximizing the signal from both single-sided outputs and setting the differential signal to almost zero. Additionally the transmittance of intensity through the optical setup was maximized using a power meter.

### PID controller

The differential signal is fed to a SRS SIM960 PID controller. Its output is connected to the modulation input on the SRS LDC501 using a voltage divider. The divider is built using three resistors of  $560\text{ k}\Omega$ ,  $11\text{ k}\Omega$  and  $430\Omega$  with 5 % tolerance each. This yields an attenuation factor of  $0.0200^{+0.0021}_{-0.0019}$  with maximum systematic uncertainties due to the resistors' tolerances. A voltage divider became necessary as the PID's output signal of  $\pm 10\text{ V}$  would result in diode-current changes of  $\pm 250\text{ mA}$ . Consequently, the attenuation factor of 0.02 allows to use a broader range of PID parameter values, enabling the PID to fine-tune the diode-current. The LDC is configured to operate in low range (0 mA to 250 mA) and low bandwidth mode (DC – 10 kHz) for lowest output noise and low range for the modulation transfer function in continuous current (CC) mode ( $25\text{ mA V}^{-1}$ ) [28].

Three universal power supplies with adjustable output voltage were chosen as a cost-saving way to provide the PID with  $\pm 15\text{ V}$ ,  $5\text{ V}$  and a common ground. A shielded cable is used to connect these wires with the female DB-15 connector. The direct interface cabling, i.e. connecting the PID controller to a RS-232 port using a DB-9/F was assembled using a ribbon cable with the computer ground connected to the signal ground. Table C.4 shows the wiring and pin assignments for both cables.

From the input/measure signal and internal or external setpoint the PID controller calculates an error signal  $\varepsilon \equiv \text{SETPOINT} - \text{MEASURE}$ . The term PID stands for the three control paths *proportional*, *integral* and *derivative*. These three paths make up the final output signal [29],

$$\text{OUTPUT} = P \left( \varepsilon + I \int \varepsilon dt + D \frac{d\varepsilon}{dt} \right) + \text{OFFSET}, \quad (3.1)$$

with the overall gain  $P$  and the path gains  $I$  and  $D$ . Parameter  $P$  leads to an output signal that is proportional to the current difference between measure and setpoint, thus being the most important control path in many applications. However, with it as the only control path, the error will most likely not reach zero. One could either apply a permanent offset, as noted in equation 3.1, or use an integral path that is a measure for the history of the error signal. Is the parameter  $I$  chosen appropriately, the error's offset will decrease dynamically. Since the weight of one data point is small in the

### 3. Experimental setup

---

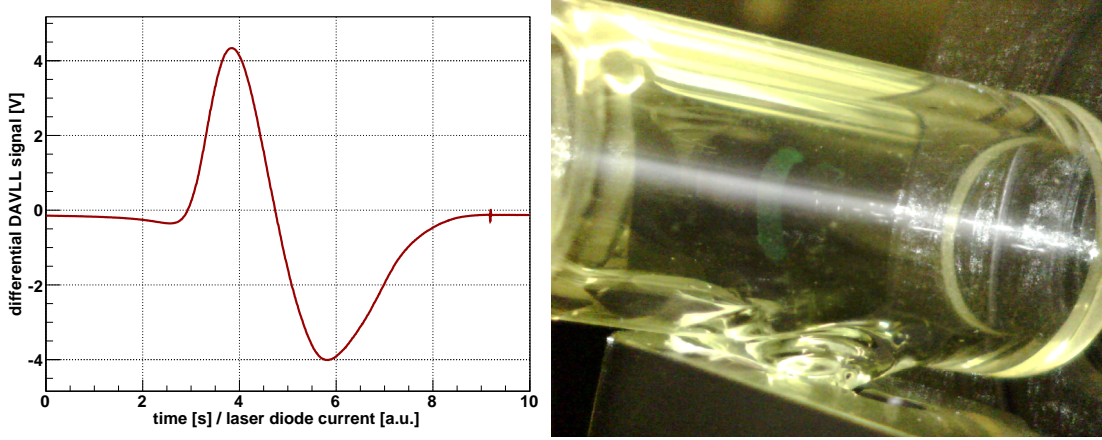


**Figure 3.8.:** Cesium fluorescence from the  $F = 3 \rightarrow F'$  transition as seen by a visible+infrared light camera (right) and as the differential signal from the DAVLL's polarimeter board (left). The LDC's RAMP command was used to make a laser current scan. The center of the DAVLL curve is found at approximately 201.70 mA depending on the DAVLL cell temperature.

integral path, it sometimes is important to also use the derivative path, which tries to anticipate changes in the input signal by calculating the current derivative of the error signal. In the setup discussed here the derivative path was disabled, because it led to immense oscillations even with  $D$  being at its minimum.

#### 3.3.3. LDC and PID parameter tuning

To operate the DAVLL and make it possible to lock using the differential signal's slope one has to estimate or measure parameters. These include the LDC's laser diode current and temperature, both of them change the emitted wavelength. With the PID controller, suitable values for the gain parameters  $P$  and  $I$  have to be found.

The temperature setpoint for the LDC's TC element was set to 32 °C. To find the wavelength for the  $F = 4 \rightarrow F'$  transition in cesium, a glass cell filled with cesium vapor was put into the beam path and monitored using a camera for visible and infrared light. Then the laser diode current was manually increased starting at 50 mA up to 230 mA. At around 201.7 mA the transition was observed (see fig. 3.8). Also cesium's  $F = 3 \rightarrow F'$  was observed at approximately 194.3 mA. This corresponds to a wavelength difference of  $\Delta\lambda \approx 22.28$  pm. A laser diode current scan using the LDC's internal ramp function was performed using a Python script talking to the LDC via its serial port. Figure 3.8 (right) shows the result of such a scan around the desired lock frequency.

From figure 3.8 it is apparent that a positive change in laser diode current, which is proportional to the time unit in that plot, leads to a decreasing signal (lock-point on the slope). Thus, the feedback of the control loop has to be negative. The polarity,  $\text{sgn}(P) = -1$ , was chosen accordingly. To find the PID's working range the (absolute)

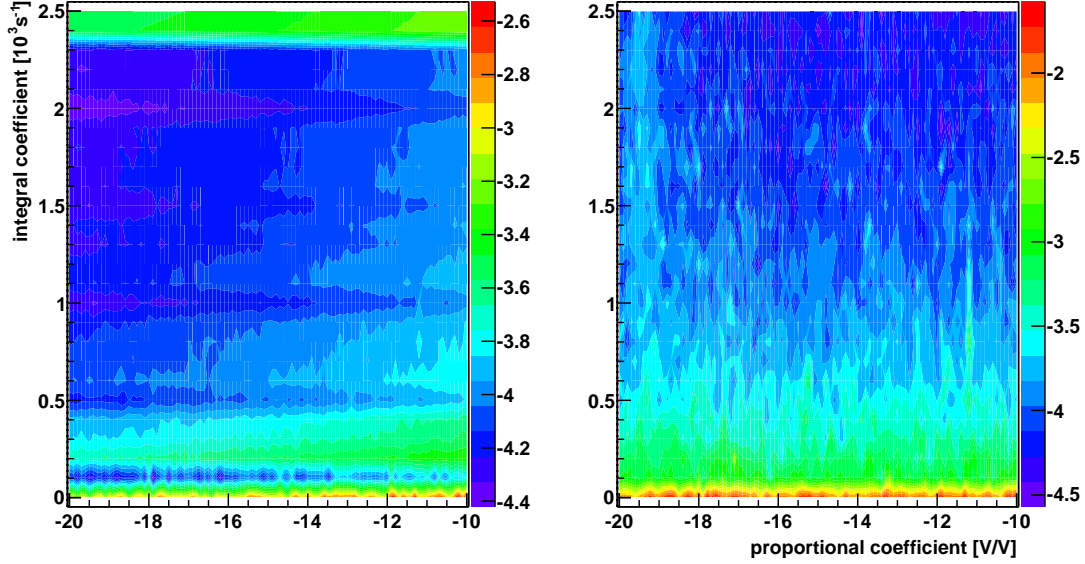


**Figure 3.9:** PID parameter scan for *proportional* and *integral* control paths. The color scale is logarithmic, with  $\log_{10}\langle\epsilon\rangle$  and  $\log_{10}\sigma_\epsilon$  on the left and right side respectively. Violet and blue colors represent small and desirable values whereas green and red correspond to parameter pairs that lead to offsets and/or fluctuations.

values for  $P$  and  $I$  were increased manually. For only *proportional* operation, the output started heavy oscillations at about  $P = -22 \text{ V/V}$ , with the lowest stable operation point around  $P = -19 \text{ V/V}$ . The same procedure was employed for  $I$ . However, there was a broad range of values with  $\mathcal{O}(I) \sim 10^3 \text{ s}^{-1}$  that allowed stable operation.

To experimentally find suitable values for operation a parameter scan in  $P$  and  $I$  was performed, measuring the error signal  $\epsilon$  several times to receive both,  $\langle\epsilon\rangle$  and  $\sigma_\epsilon$ . Figures 3.9 and B.3 show such a scan with  $\langle\epsilon\rangle$  and  $\sigma_\epsilon$  on a logarithmic scale with basis 10. Using both values, one could rule out the use of small  $\langle\epsilon\rangle$  with high fluctuations. Subsequently, three parameter value pairs were chosen for further investigation,  $([P], [I]) \in \{(-19, 1000), (-19, 2000), (-12.2, 2000)\}$ .

Several measurements of both, the PID input and output have been made to assess which parameter set yields the lowest standard deviation for the output signal. For stationary input signals the lowest signal standard deviation was found for  $P = -19 \text{ V V}^{-1}$  and  $I = 2000 \text{ s}^{-1}$ . Hence this parameter set was chosen for operation.

### PID-induced laser wavelength noise

With only the proportional channel in use the PID's output is likely to oscillate around the ideal value with a finite amplitude. Using the integrating channel this amplitude is vastly reduced. However, small oscillations remain. At small amplitudes other sources

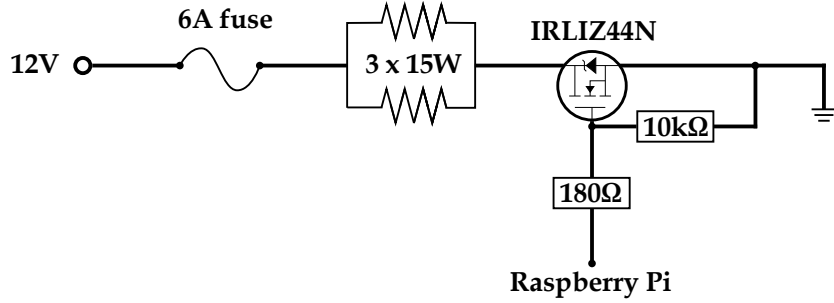


**Figure 3.10.:** Wiring diagram for the Raspberry Pi controlled temperature stabilization of the DAVLL system. Three 15 W heat pads are used for heat generation. There is no active cooling mechanism.

of noise also contribute to the overall noise level. Under normal conditions the PID controller's output was recorded after the voltage divider. Recording was done using an oscilloscope sampling at 100 MHz for 100 ms and different bandwidths.

Integrating over the power spectral density yielded a total noise of 0.70 mV and 0.52 mV for full and 20 MHz bandwidth respectively. With the LDC501's modulation factor of  $25 \text{ mA V}^{-1}$  and the laser diode's wavelength dependence  $d\lambda/dI = 0.003 \text{ nm mA}^{-1}$  [30] this translates into  $\Delta\lambda_{\text{full}} = 53 \text{ fm}$  and  $\Delta\lambda_{20 \text{ MHz}} = 39 \text{ fm}$ . This change is more than six orders of magnitude smaller than the transition wavelength itself and thus negligible.

### 3.3.4. Thermal stabilization

The cesium vapor inside the DAVLL cell is sensitive to changes in temperature, influencing its vapor pressure [27]. The higher this pressure is the more cesium atoms are evaporated into the glass cell's volume, thus changing the optical absorption of light. The DAVLL's setpoint is ideally set to zero, which corresponds to the frequency  $f_{D_2}$ . However, small deviations are almost inevitable. As the absorption gets bigger due to more cesium inside the cell, the lock curve changes, i.e. it gets steeper. This mismatches frequencies and curve values compared between different vapor pressures. This effect is qualitatively shown in figure 3.8. Changes in temperature also cause the Doppler-broadening to be bigger. However, the cesium's vapor pressure is more sensitive to small changes than the Doppler-broadening. Additional sources of error include temperature dependencies of optical elements and the polarimeter board.

It is thus required to provide a nearly constant temperature to the DAVLL system. This is done using three 15 W heat pads and a bended copper plate for thermal conduction and promoting an equal and fast distribution of heat. The heating is controlled by pulse width modulation (PWM) on a Raspberry Pi using a MOSFET transistor (IRLIZ44N) that is designed to operate at drain-currents up to 30 A with a breakdown voltage of 55 V. Temperature control is employed by using three DS18S20 digital thermometers distributed equally from the initial  $\lambda/2$ -plate to the  $\lambda/4$ -plate.

These sensors are also being read by the Raspberry Pi and their values being averaged. Figure 3.10 shows the wiring for the heating circuit.

A software PID written in Python controls the PWM and thus the heating depending on the temperature. The PWM-frequency is set to 50 Hz. Using the proportional and integrating channel an output between 0 % and 100 % is calculated. The integral is calculated using the trapezoidal rule on the current and 24 previous temperatures. It is switched off as the temperature reaches the setpoint and back on again as it drops below. Additionally the register for previous temperatures is cleared. Due to the lethargy of the system falling temperatures need to be countered before the system's temperature drops well below the setpoint. Thus the PID's differential channel is switched on for temperatures 1 K higher than the setpoint. Since this system is designed to only heat, care was taken to choose the PID parameters and also the register size appropriately. Storing 25 values and using  $P = 10$ ,  $I = 2.5$  and  $D = -0.05$  proved to be effective for stabilization.

Log files show that the heating and software PID keep the system stable within  $0.6^\circ\text{C}$  at  $35^\circ\text{C}$  for more than six hours. Using the curve in Steck (2010) [26] the temperature vapor pressure's dependence can be calculated to be approximately  $0.4 \times 10^{-6}$  torr/ $^\circ\text{C}$  at  $30^\circ\text{C}$ . This translates  $0.6^\circ\text{C}$  into  $0.24 \times 10^{-6}$  torr, changing the vapor pressure by 4 %. The oscillations seen in figure B.4 appear on a timescale of several seconds. However, the goal of preventing any long-term drift succeeded as the temperature is kept at the preset level within the stated range for several hours of operation.

### 3.4. High voltage electrodes and shielding

The layout for the high voltage electrodes was determined by the necessity for the laser to travel through the electrodes themselves and by the aim to create an electric field as homogeneous as possible for the area of the quartz crystal. A cylinder was chosen with its lateral surface rounded. It has a radius of 49.5 mm and is 9 mm thick. A 3 mm wide hole is drilled into the center. Additional features are two 4 mm wide holes for attachment of the crystal holder using M4 screws and a M6 thread hole for secure attachment of either the high voltage or ground cable. Every hole's edges were rounded to minimize spikes and thus high voltage breakdowns. Figure B.5 shows a sketch of such an electrode from the back.

The crystal holder seen in figure 3.11 between the electrodes also functions as a holder for them. This was chosen to minimize the space for air in between the electrodes and other parts as well as to properly align crystal and electrodes along one common axis. The quartz holder was 3D printed with acrylonitrile butadiene styrene (ABS) plastic as material. A sketch for the holder is shown in figure B.6.

A simulation for the electric field inside the electrodes was done using COMSOL®. The simulation features the quartz crystal inside its holder attached to two electrodes

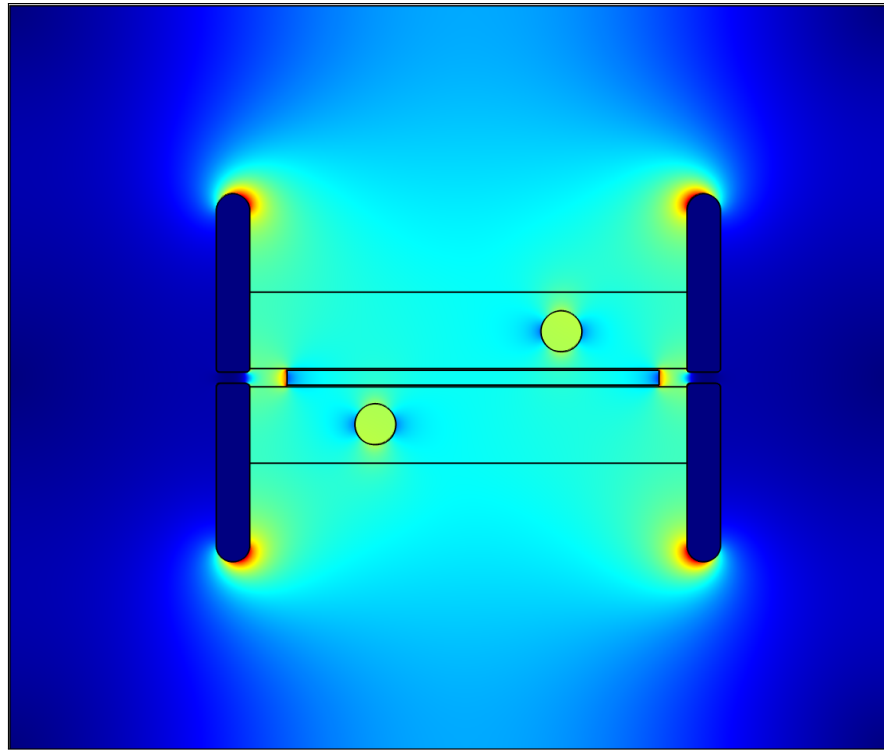


**Figure 3.11.**: Electric field simulation using COMSOL® featuring a quartz crystal in its acrylonitrile butadiene styrene (ABS) plastic holder in between two electrodes. The assembly is put inside a grounded box filled with air at normal conditions. The color range extends from  $0 \text{ kV mm}^{-1}$  to just over  $2 \text{ kV mm}^{-1}$ .

one of which is on high voltage inside a grounded box filled with air. The results show that the highest field is located at the electrodes' edges and at both ends of the crystal. However, for a maximum voltage of  $10 \text{ kV}$  the resulting field is  $\sim 2 \text{ kV mm}^{-1}$ , which is lower than the breakdown condition in air. Using the simulation the chosen dimensions for electrodes and crystal holder were validated. Figure B.7 is a snippet of the simulation and shows the field near the quartz crystal's edges inside the holder.

The electrodes and holder are enclosed in a Faraday cage made from of aluminum plates, which are screwed together. Two side plates feature two holes, one for the laser beam and one for the ground and high voltages cable respectively. A PVC plate serves as insulation between the cage and the breadboard. However, the breadboard as well as all aluminum plates are connected to the same ground, which is also the ground used for one of the electrodes. The final high voltage assembly is shown in figure 3.12 as a rendered image. For photographs of the setup see the appendix B (fig. B.9).

The electrodes are connected to a Trek 610E high voltage power supply that delivers up to  $10 \text{ kV}$  with positive or negative polarity. It can be operated as a high voltage reference supply and amplifier. The first uses the front panel input to set a voltage

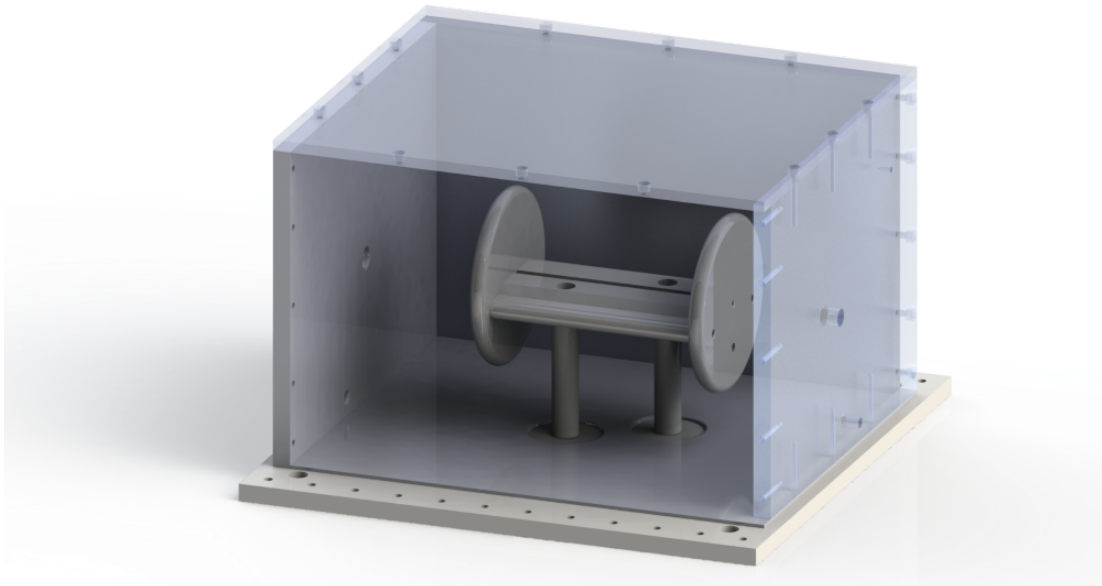


**Figure 3.12.:** SolidWorks® rendered image of the final high voltage assembly consisting of PVC breadboard, Faraday cage, 3D-printed crystal holder and posts and electrodes made from aluminum.

while the latter amplifies an input signal. Thus, it's possible to modulate the high voltage using a function generator.



# CHAPTER 4

---

## Software development

The scripts and software that were developed during this thesis consist of Python scripts and C++ programs sharing a common library. The code is available to the workgroup and on request. Due to the amount of code it is only printed in snippets in this thesis.

The shared library contains modules for I/O, data manipulation, string and specialized operations such as filtering and window functions. A description of each file's contents is given in table C.1. Calculating the Fourier transform of discrete data is done using the discrete fourier transform (DFT) [31] algorithms (R2C and C2R) provided by the Fastest Fourier Transform in the West (FFTW) project.

Basis for all programs are waveform files recorded by an oscilloscope and read by a Python script. Their format is given in table C.5.

### 4.1. Segmented discrete Fourier transform analysis

The implementation of the segmented fast fourier transform (FFT) algorithm is based on Heinzel et al. (2002) [31]. It is coded in C++ and extends the shared library by a template class that can distinguish between float, double and long double.

The purpose of this program is to calculate a frequency spectrum both for amplitude and noise estimation also known as linear spectrum (LS) and linear spectral density (LSD). First, the mean of the input data is subtracted it, to minimize the DC contribution, which is necessary to improve the resolution at low frequencies. Then the data is cut into overlapping segments with their sizes depending on the chosen frequency resolution. The overlap is necessary because window functions (see below) tend to suppress data on both ends of their range [31]. For each window function an ideal overlap was taken from the paper by Heinzel et al. The number of segments should be well above ten.

To improve either the sensitivity for peak or amplitude resolutions, a broad range of windows can be used, e.g. Hamming, Nuttall or flat-top windows. The segmented data is multiplied by the window values and two measures,  $S_1$  and  $S_2$  are calculated. They are used to correctly scale the DFT results. Together with the sampling frequency and number of data points they also define the effective noise bandwith (ENBW) and normalized equivalent noise bandwith (NENBW).

#### 4. Software development

---

```
1  typedef float DTTYPE; // float, double or long double
2
3  int main(int argc, char *argv[], char *envp[]) {
4      char *ifname;
5      DTTYPE fs, fr;
6      string window = "HAMMING";
7
8      const WINDOW_TYPE wdw_type =
9          → Windows<DTTYPE>::ParseWindowType(window.c_str());
10     const float wdw_overlap = Windows<DTTYPE>::IdealOverlap(wdw_type);
11
12     // READ DATA AND CONVERT IT
13     WaveformHeader header;
14     vector<DTTYPE> data;
15     vector<byte> data_byte = File::ReadBINARY(ifname);
16     ConvertRecordedWaveform(data_byte, data, header);
17
18     // subtract the data-mean to reduce DC-impact
19     DTTYPE mean;
20     mean = std::accumulate(data.begin(), data.end(), (DTTYPE)0.0) /
21         → data.size();
22     std::transform(data.begin(), data.end(), data.begin(),
23         → std::bind1st(std::minus<DTTYPE>(), mean));
24
25     // Create the core, segmentize and run it
26     SegmentedFFT<DTTYPE> *fft = new SegmentedFFT<DTTYPE>(&data, fs, fr,
27         → window, wdw_overlap, true);
28     fft->Segmentize();
29     fft->FFTEexecute();
30
31     // Create byte vector with header info + data
32     vector<byte> fft_byte = fft->ToByte();
33     File::WriteBINARY(String::ReplaceExtension(ifname, "bin.out").c_str(),
34         → fft_byte);
35
36     delete fft;
37     return 0;
38 }
```

**Listing 1:** Program body for using the `SegmentedFFT<T>` class. It uses windows for data manipulation to enhance amplitude or frequency resolution. The segmentation reduces the statistical uncertainty. Both enhancements are done at the cost of slight correlation between adjacent frequency bins.

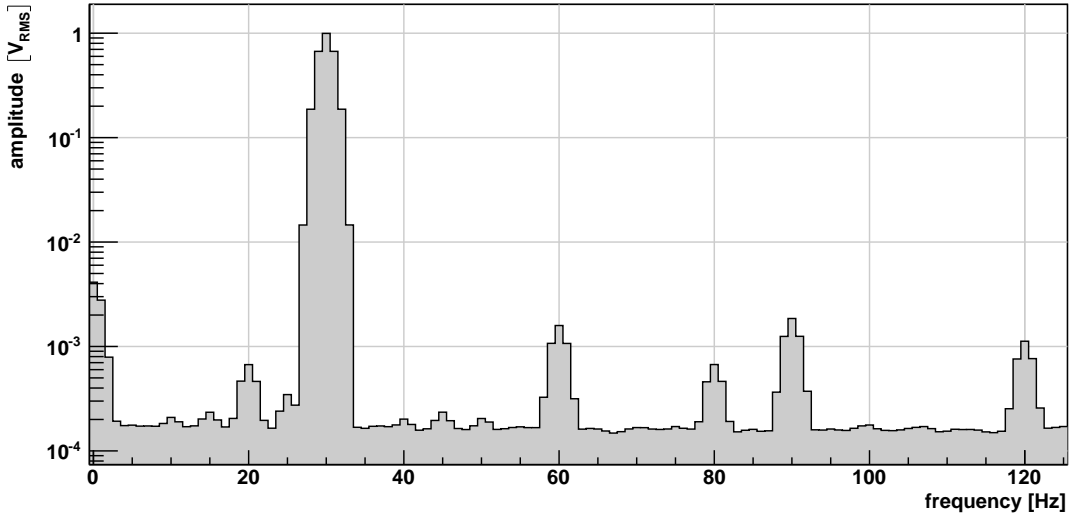


**Figure 4.1.:** Segmented discrete Fourier transform of a generated 30 Hz sine wave with 1 V<sub>RMS</sub> amplitude. Also higher harmonics were measured. During the analysis the Nuttall4C window was used.

The program used in this thesis is basically the code shown in listing 1. First the waveform data is read and converted as it also contains header data. Then the data's mean is subtracted before a `SegmentedFFT<T>` object is created, which segments the data, multiplies them with the window values, calculates each DFT and averages them. The result is converted to a byte array which together with some information, e.g. about the sampling frequency and ENBW, is written to a file. The format, i.e. byte assignment of the binary file is shown in table C.6.

To verify the validity of the program's output both, the analysis of simulated data and more important of actual measured data was performed. For the latter a sine wave with 1 V<sub>RMS</sub>, offset 1.5 V and frequency 30 Hz was generated using a Stanford Research Systems DS345 function generator. The waveform was fed to an oscilloscope. The results of a segmented DFT are shown in figure 4.1, clearly showing a peak with 1 V<sub>RMS</sub> at 30 Hz. In addition to that peak also higher harmonics at 60 Hz, 90 Hz and 120 Hz are visible.

## 4.2. Software lock-in amplifier

Lock-in amplifiers can detect very small signals which otherwise blur into much bigger signals. They use phase-sensitive detection to filter the signal with respect to a specific frequency and phase using an internal reference [23]. A signal  $V_S$  multiplied by the (lock) reference  $V_L$  yields

$$V_{PSD} = \frac{V_S V_L}{2} \{ \cos ((\omega_S - \omega_L) + \phi_S - \phi_L) - \cos ((\omega_S + \omega_L) + \phi_S + \phi_L) \},$$

#### 4. Software development

---

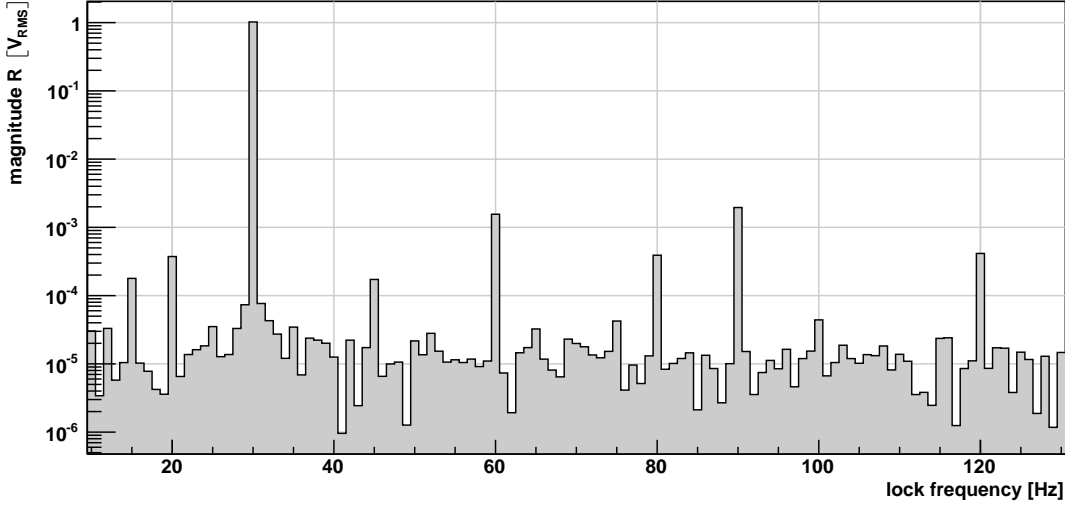


**Figure 4.2.:** Software lock-in scan from 10 Hz to 130 Hz with 1 Hz resolution. The low-pass transition frequency was set to 0.1 Hz. As with the segmented DFT the results show the 30 Hz oscillation with 1 V<sub>RMS</sub> and its higher harmonics.

which is a combination of two cosines with frequencies  $\Delta\omega = \omega_S - \omega_L$  and  $\omega_S + \omega_L$ . For  $\Delta\omega \approx 0$  low-pass filtering with a very low transmission frequency gets rid of the second cosine and leaves [23]

$$V_{\text{PSD}} = \frac{V_S V_L}{2} \cos(\phi_S - \phi_L) .$$

Multiplication with the lock-reference shifted by  $\pi/2$  yields the same, but with a sine function. From that two values,  $X = V_S \cos \Delta\phi$  and  $Y = V_S \sin \Delta\phi$  are calculated, which combined yield the phase-insensitive magnitude

$$R = \sqrt{X^2 + Y^2} = V_S .$$

The algorithm's implementation consists of the multiplication of the datasets with the reference sine and cosine functions and subsequent low-pass filtering of the data sets. The filters are calculated using the Fourier transform of the sinc function, using a Hamming windows as default. The convolution of filter and data is done as a multiplication in the frequency domain. The resulting data is then transformed back into the time domain. Using the `LockIn<T>` class in a program differs from the `SegmentedFFT<T>` only in the actual usage of the class and the output method (see lst. 2). The output consists of three equally long lists containing the lock-frequencies, calculated magnitudes and phases (see tab. C.7).

This algorithm was also tested using the recorded 30 Hz waveform with 1 V<sub>RMS</sub>. The results for a scan performed on frequencies from 10 Hz to 130 Hz are shown in figure 4.2. The main peak as well as higher harmonics are easy to identify.

```

1  typedef float DTTYPE; // float, double or long double
2
3  int main(int argc, char *argv[]) {
4      /*
5      . . .
6      */
7
8      vdata = CropData(vdata, crop_group);
9      hdr.N /= crop_group; fs /= crop_group; fn = fs / 2;
10
11     if (fl_res <= 0) fl_res = (DTTYPE)(fs / hdr.N) * crop_group;
12     if (fl_low < 0) fl_low = (DTTYPE)(fs / hdr.N);
13     if (fl_high < 0) fl_high = (DTTYPE)(fn);
14     const size_t n = (size_t)((fl_high - fl_low) / fl_res) + 1;
15
16     vector<LockInReturn<DTTYPE>> rt;
17     rt.reserve(n);
18
19     for (i = 0; i < n; ++i) {
20         DTTYPE tmp_fl = i * fl_res + fl_low;
21         rt.push_back(LockIn<DTTYPE>::CalculateLock(vdata, hdr, fs, tmp_fl, ft,
22             → false));
23     }
24
25     size_t i;
26     vector<DTTYPE> _fl, _Ravg, _PH;
27     _fl.resize(n); _Ravg.resize(n); _PH.resize(n);
28     for (i = 0; i < n; ++i) {
29         _fl[i] = rt[i].flock;
30         _Ravg[i] = rt[i].Ravg / (DTTYPE)hdr.N;
31         _PH[i] = rt[i].PHASE;
32     }
33
34     vector<byte> bout; vector<DTTYPE> fout;
35     fout.assign(_fl.begin(), _fl.end());
36     fout.insert(fout.end(), _Ravg.begin(), _Ravg.end());
37     fout.insert(fout.end(), _PH.begin(), _PH.end());
38     bout = ConvertToByteVector(fout);
39     File::WriteBINAY(String::ReplaceExtension(ifname, "bin.lock").c_str(),
40             → bout);
41
42     return 0;
43 }
```

**Listing 2:** Program body for using the LockIn<T> class. It calculates the magnitude in a range of  $\pm 20\%$  around the desired lock-frequency. A second similar code was written to perform a wider scan depending on input parameters for frequency range and resolution.



# CHAPTER 5

## Measuring the electric field induced Pockels effect

After extensive work on the setup's alignment and mechanical stability initial measurements with high voltage were performed. The voltage was gradually increased to 10 V with a subsequent change to  $-10$  V validating that the setup could be operated at those voltages and with sudden changes to them.

From equation 2.3 it is evident that the magnitude is scaled depending on the angles  $\vartheta$  and  $\tilde{\vartheta}$  which are related to both the quartz crystal's optical axis and the Wollaston prism's alignment with regard to the initial rotation of the polarization plane. Thus, by rotating the crystal along the cylinder axis the magnitude of the Pockels effect can be changed. If an absolute field measurement is desired, the coefficients  $c(\vartheta, \tilde{\vartheta})$  and  $s(\vartheta, \tilde{\vartheta})$  in 2.3 have to be estimated or determined after each adjustment of either the Wollaston prism, quartz crystal or polarizer (see sec. 5.2). For measuring absolute differences between field strengths the formula can be simplified yielding equation 2.4 where only the general coefficient hast to be determined once.

### Sudden changes in high voltage

As a first test of the setup the voltage was switched on from 0 kV to  $\pm 10$  kV. A change of the polarization plane induced by the Pockels effect would lead to a change of the differential signal at the measurement board.

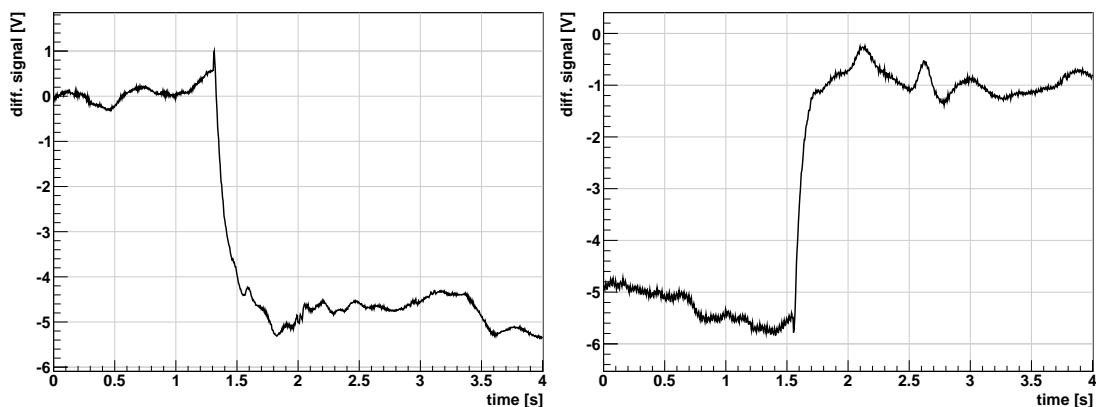


**Figure 5.1:** Rotation of polarization plane measured as differential signal by the polarimeter board. The high voltage was switched on from 0 kV to 10 kV and vice-versa. The process for negative polarity (0 kV to  $-10$  kV) is shown in figure B.12.

Figure 5.1 shows the effect of changing the applied voltage from 0 kV to 10 kV. The differential signal changes by approximately 5 V, thus translating the range of  $\pm 10$  kV into roughly  $\pm 10$  V. This proved that it is possible to measure electric fields using the Pockels effect in quartz. However, unpredictable changes and drifts on a timescale of 100 ms and larger were also observed. These were first attributed to the at that time not yet thermally stabilized DAVLL. However, after rearranging the setup and installation of the temperature stabilization still some drifts remained.

## 5.1. Oscillating electric fields

One of the most effective ways to improve a measurement's resolution is to turn it into a frequency measurement, since frequencies can be measured very precisely. Either hardware like lock-in amplifiers or software is used to process the measured data and extract the frequency information. For this thesis both, segmented discrete Fourier analysis and software lock-in algorithms were used for data processing (see cha. 4).

The Trek 610E high voltage supply features an external input on its rear side and can be operated as a high voltage amplifier [32] enabling it to create an oscillating voltage on the electrodes. The amplifier's gain is chosen to be 1 kV/V. For input generation, again a Stanford Research Systems DS345 function generator is used. If not stated otherwise, a sine function with zero offset is used. For verification that any signal seen at the driving frequency is solely due to the oscillating high voltage the setup is switched on but does not pass high voltage on to the electrodes (switch operated). For a generated signal of  $10\text{ V}_{\text{pp}}$  at 10 Hz the results of both the segmented DFT and software lock-in were negative (see fig. B.8). This means that no signal was found at 10 Hz with an amplitude greater than  $10\text{ mV}_{\text{RMS}}$ .

### 5.1.1. Background signals in the frequency domain

As the spectrum taken for the previous test does not deviate from other recorded background spectra it is used as such. The large increase of the noise floor at frequencies below 100 Hz is attributed to mechanical vibrations caused by the air ventilation system of the room where the experiment is set up. This claim is supported by a measurement of the background spectra with running fans and after disabling them for several minutes. The results of the segmented DFT analysis are shown in figure 5.2. Without running fans the increase of the noise floor now starts at 10 Hz, but remains more than one order of magnitude below the original one. Unfortunately switching off the ventilation system is not feasible as the temperature inside the room increases rapidly, thus influencing the highly sensitive components (e.g. wave plates). An additional background feature is a cluster of signals oscillating at frequencies at around 30 Hz and from 40 Hz to 100 Hz. The amplitude is reproducible across the

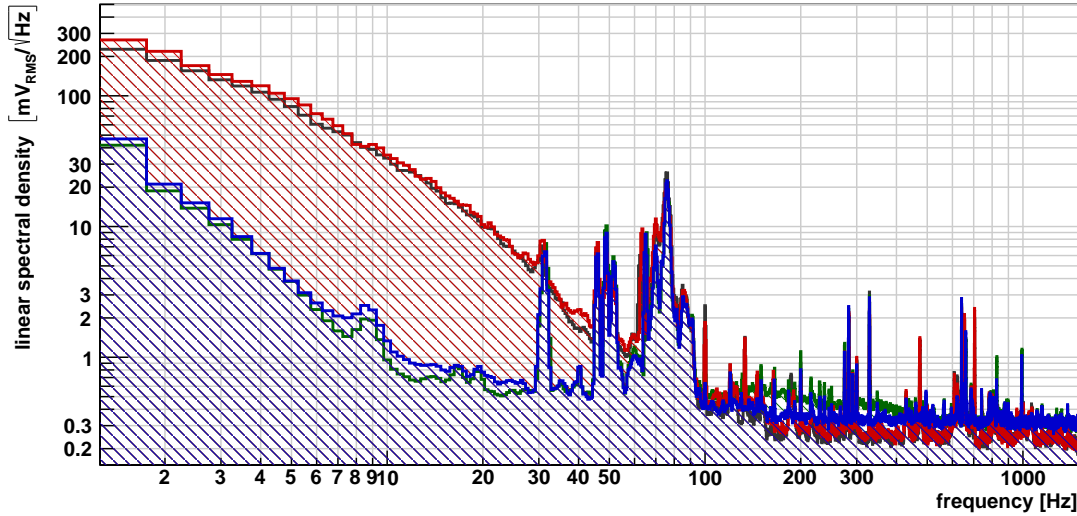


**Figure 5.2.:** Spectral background in the frequency domain of the setup for running (red, gray) and switched off (blue, green) ventilation system. Data was acquired over a 100 s interval with 100 kHz sampling rate. This is a truncated view (up to 1.5 kHz) of the whole spectrum, which ranges up to 50 kHz. A Nuttall4C window was used with a NENBW and ENBW of 1.976 bins and 0.988 Hz respectively.

four performed measurements and thus can be regarded as stationary. When analyzing signals in this region the background peaks and their possible interference have to be taken into account.

Additional measurements were made to assess the origin of this cluster. During those the polarimeter board was screened using laser light absorbing foil. Each measurement was performed with the ambient light switched on and off. With no laser beam the difference in the range from 30 Hz to 100 Hz between the spectra is an enhanced noise level below 1 Hz, a higher peak at 50 Hz and a significant one at 100 Hz induced by the ambient light and its electronics (see fig. B.13). As the cluster of signals was absent with no laser light it can be concluded that there is no significant pick-up of noise from the polarimeter board. The frequency spectrum of the DAVLL output measured after the voltage divider (fig. B.14) showed broad peaks at 30 Hz, 50 Hz and 30 Hz aside from peaks at higher orders of magnitudes. However, the amplitude at those frequencies is several orders of magnitude smaller than those seen in the signal cluster, but the LDC's transfer function of 25 mA/V has to be factored in. Thus, it is reasonable to assume that the system of DAVLL, LDC and the wiring involved plays a major role in the creation of the observed cluster.

### 5.1.2. Frequency transfer - capacitance limited maximum field

Initially, measurements with four different modulation frequencies (10 Hz to 40 Hz) and amplitudes ( $5 \text{ V}_{\text{pp}}$  and  $10 \text{ V}_{\text{pp}}$ ) were performed. Figure 5.3 shows both modu-

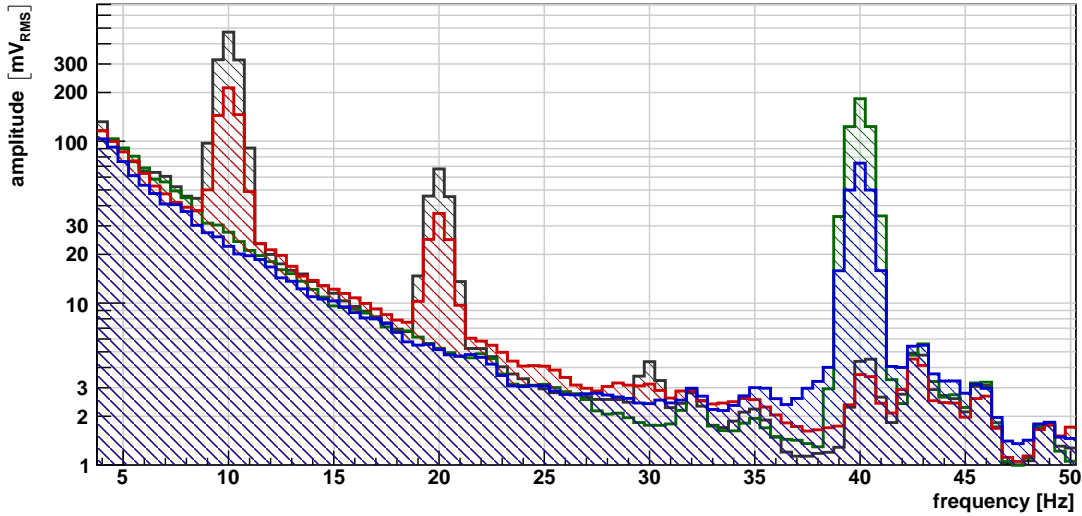


**Figure 5.3.:** Frequency spectra from modulating the high voltage with 10Hz and 40Hz sine waves. Both for different amplitudes of 5kV (red, gray) and 10kV (blue, green). The second order harmonic of 10Hz is also visible. The decrease in amplitude is related to the electrodes acting as a capacitance. A Nuttall4C windows was used in the calculation.

lation amplitudes for frequencies 10Hz and 40Hz for comparison. As expected the peak height increases with higher voltages, while it decreases for higher frequencies. This decrease is mainly due to the electrode setup acting as a capacitor with a finite time constant. The decrease occurs when the time to collect the appropriate amount of charges to create a potential that matches the supply voltage is higher than one quarter of the modulation period. Over the range of measured frequencies this effect is significant as the signal amplitude decreases from 214 mV<sub>RMS</sub> to 73 mV<sub>RMS</sub> and 472 mV<sub>RMS</sub> to 183 mV<sub>RMS</sub> for 5 V<sub>pp</sub> and 10 V<sub>pp</sub> modulation amplitude respectively (see fig. 5.3). The effect of incomplete charging, related to the saturation curve  $1 - e^{-t/\tau_{RC}}$  manifests itself in a proportionality to  $e^{-t/\tau_{RC}}$ . This is also seen when plotting the amplitude values extracted from the Fourier transforms over modulation frequency (see fig B.15).

### 5.1.3. Amplitude calculation

The laser intensity is measured using a power meter on the beam before it passes through the Wollaston prism. Assuming a transmittance of 94 % the total beam intensity behind the prism is approximately 277  $\mu$ W. The function generator is set to 10 Hz with 10 V amplitude creating an oscillating high voltage of  $\pm 10$  kV at gain 1 kV/V). A time series was acquired at a sampling rate of 100 kHz for 100 s and analyzed using the segmented DFT algorithm with 0.5 Hz frequency resolution and the Nuttall4C window. A snippet of the results is shown in figure 5.4 with the main peak at 10 Hz and the first higher harmonic at 20 Hz. The main peak is 65.34 mV<sub>RMS</sub> high, applying a factor of  $2\sqrt{2}$  yields the peak-to-peak value of 184.81 mV<sub>pp</sub>.

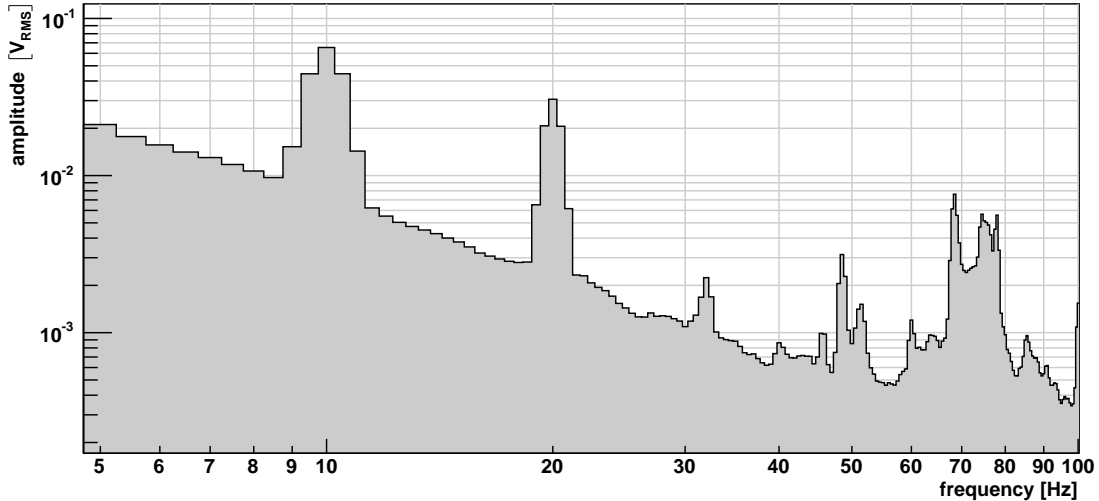


**Figure 5.4.:** Segmented DFT results for high voltage modulation with 10 kV and 10 Hz frequency (sine). The main peak at 10 Hz is 65.34 mV<sub>RMS</sub> high. The spectrum was created using a Nuttall4C window and 0.5 Hz frequency resolution.

Using the linear model from equation 2.4 and the value for the slope  $\eta$  calculated in the next section a peak-to-peak value of 184.81 mV<sub>PP</sub> corresponds to a change in high voltage of 18.481 kV. This value is close to the setpoint of 20 kV. However, the capacitance effect of the electrodes described in the previous section can be seen to have a significant effect. At 10 Hz the achieved high voltage difference is already lowered by more than 1.5 kV.

## 5.2. Measuring absolute field values

The goal set to achieve with this setup and experiment is to measure the stability of the electric field down to 10<sup>-4</sup> of 18 kV cm<sup>-1</sup>. This means keeping track of changes to it over time. However, even from observation of the differential output's behavior with the bare eye it is evident that a high-resolution stability measurement can not be achieved as of now. For such purpose the signal fluctuations, primarily due to the necessary ventilation system, are too big. To contain the signal well within the polarimeter board's range (output between ±8 V) the maximum laser intensity needs to be reduced. However, a higher intensity would greatly help countering the rather small linear electro-optic coefficient of quartz. Despite this it is worthwhile to investigate which performance can be achieved by the setup.

The response to a field change can be calculated from equation 2.3 or better 2.4. The coefficients in front of the electric field difference are constant for a specific alignment of polarizer, crystal and Wollaston prism. The equation thus can be reduced to  $\Delta(A, B) := \eta \cdot (E_B - E_A)$ , leaving only the slope  $\eta$  to be determined. With approximately 277 µW of light that gets transmitted through the Wollaston prism and a differ-

ential signal change of 200 mV for  $\Delta U_{\text{HV}} = 20 \text{ kV}$  the slope is  $6.44662 \times 10^{-10} \text{ m kV}^{-1}$ . The acquired signal looks similar to the one seen in figure 5.5. This slope-value can certainly be increased with further adjustments of the crystal's rotation. However, a larger coefficient may also increase the effect of external influences.

The beam intensity above was measured using an external power meter measuring the intensity before passing through the Wollaston prism. However, it would be advantageous to measure the incident light intensity using the polarimeter board itself to have access to an internal calibration measure. Unfortunately this is only possible for intensities below  $28.5 \mu\text{W}$  of either or both of the polarized beams that hit the photo diodes. This threshold is calculated using the diode's spectral response of  $0.56 \text{ A W}^{-1}$  [22] and the amplification value of  $499 \text{ V mA}^{-1}$  for each of the single-sided paths.

### 5.2.1. Semi-static electric field changes

To check the validity of equation 2.4 the function generator was set to create a low frequency step function with an amplitude of 5 kV thus resulting in a total step of 10 kV. A part of the acquired image is shown in figure 5.5. The scales are as indicated 200 mV/div (yellow), 5 kV/div (green) and 1 s/div on the time axis. One can clearly identify the discrete steps in the signal. Additionally, the difference between the first lower and second higher signal (both yellow) is approximately 99 mV. Using the aforementioned linear model  $\Delta(A, B) := \eta \cdot (E_B - E_A)$ , the prediction would have been 100 mV. In light of the rather broad signal both values can be regarded as to be in agreement with each other thus validating this model.

To assess the maximum performance of this setup the step size was reduced accordingly until the signal step blended into the signal's noise. This was already the case at 2 kV, which is two orders of magnitude higher than the envisioned  $10^{-4}$  of 180 kV at 12 cm [11].

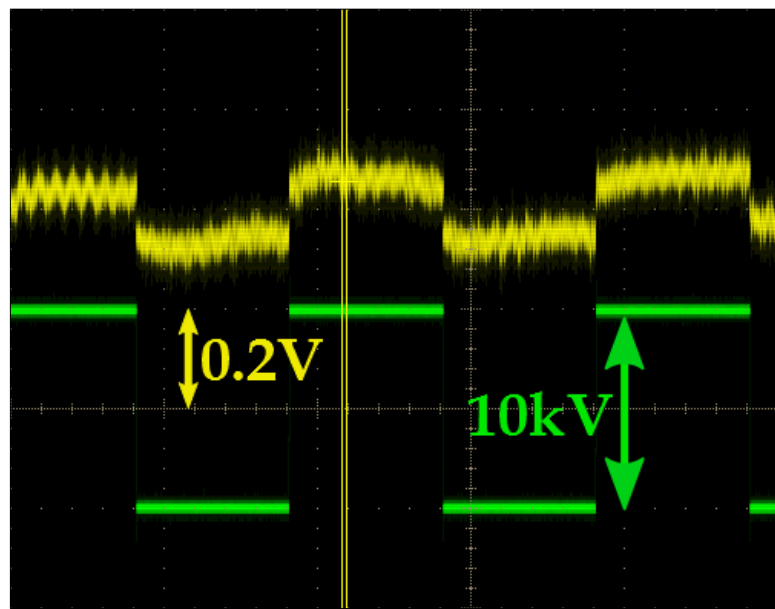


**Figure 5.5.:** Acquired differential signal in time series with a 0.5 Hz step function with step size 10 kV. The time axis is scaled in 1 s/div. The step seen in the yellow signal is approximately 99 mV.



# CHAPTER 6

---

## Test operation of 200 kV high voltage supply

The power supply used in the TUM-nEDM experiment provides a voltage of up to  $\pm 200$  kV. It was built by FuG Elektronik GmbH. One of its features is that the last percent of the supply's output is separately tunable. Setting the voltage is either done using the front panel knobs or the back panel connectors. The latter makes it possible to integrate the power supply into a feedback loop to stabilize the electric field and react to changes of it.

The supply was delivered to the experiment's site in summer 2015 and was made operational for the first time for the purpose of this thesis. Its rotating knobs on the front panel are used to set the output voltage, where the indicated range of 0 to 10 corresponds to  $\mp 200$  kV. The supply was connected to the grid using wires from an IEC power connector. Since the location and tests performed were preliminary the supply's ground was not connected to the central grounding point (CGP), but instead to the grid's grounding wire.

### High-voltage output noise

To assess and characterize the performance of the high voltage power supply the noise on its output was to be measured. After connecting all relevant contacts a time series was acquired at a very low output voltage of less than 30 V. During this a rather high 50 Hz noise was observed. To further increase the output voltage and assess whether this noise is relative, i.e. scaling with the output, a voltage divider using  $1\text{ M}\Omega$  and  $1\text{ G}\Omega$  resistors was built. This is necessary as the oscilloscope has a maximum input voltage of 30 V.

Using the voltage divider three different voltages were probed at 700 V, 3.34 kV and 5 kV with the order of magnitude being more important than the actual precise output value. At 700 V the measured voltage was oscillating around 680 mV with an amplitude of almost 700 mV which is extraordinarily high. However, it has to be taken into account that the supply was not properly grounded. Furthermore, the absolute 50 Hz amplitude decreased with increasing high voltage, thus vastly improving the output-to-noise ratio. At 3.34 kV and 5 kV the amplitude remained at approximately 500 mV. Also, using a 20 pF capacitor mimicking the properties of the final experiment also showed no noticeable effect on the noise. These points show that it is likely for the noise to decrease further as the high voltage is increased into the regime of 200 kV. Also proper grounding using the experiment's CGP will vastly reduce the 50 Hz noise as it gets decoupled from the grid.



# CHAPTER 7

---

## Conclusion and outlook

The purpose of this work was to build an experimental setup for optical electric-field measurements using the linear electro-optic effect in quartz and evaluate its performance.

Thus, during this work a completely new setup was built to use the linear electro-optic effect in quartz as a means to measure the electric field both in the time and frequency domain. This included the assembly of an optical beam path including a dichroic atomic vapor laser lock (DAVLL) system, which uses an analog PID controller whose parameters are tuned towards optimal operation. Additionally a temperature stabilizing heating-cover was assembled using a software PID to keep the DAVLL's temperature at a certain value. To measure the effect of electric fields a combined holder for both the electrodes and Pockels crystal was designed and 3D printed. The electrodes and a Faraday cage made from solid aluminum acting as a high-voltage screening were designed and the production was performed by the department's workshop. Several small polarimeter boards have been soldered in two different configurations during this thesis. They are being used by the DAVLL system and to detect the polarized beams leaving the polarizing beam splitter. Furthermore, the polarimeter board's noise was measured using a hardware lock-in amplifier.

Various Python modules and programs were created that are used for calibration tasks and for steady operation of the setup, e.g. controlling the DAVLL temperature stabilization and data acquisition from the oscilloscope. Additionally two programs were developed to aid the evaluation of the acquired raw data. A segmented discrete Fourier transform to calculate frequency spectra from a time series and a software lock-in amplifier, which can be used as a highly sensitive method to extract an amplitude at a fixed frequency or to scan a range for signals.

Successively, the rotation of the laser's plane of polarization due to the influence of electric-fields of up to 100 kV/m was measured. Both, oscillating and semi-static field changes were induced and measured. Sources of background noise in the frequency domain were measured and linked to their sources, a major contribution being the ventilation system of the room where the experiment was set up. The performance of the high-voltage supply was found to decrease towards higher modulation frequencies as the voltage build-up on the electrodes is slower than the modulation period, thus decreasing the effectively applied voltage. However, this is this solely a characteristic of the electrodes and power supply used in this work and configuration. Using the aforementioned software it is possible to detect and measure signals down to almost 1 Hz. The threshold is being determined by the duration of one acquisition segment. Mostly an acquisition time of 100 s was used. Thus, when pushing towards more segments within one measurement cycle of the TUM-nEDM experiment

## 7. Conclusion and outlook

---

( $\approx 200$  s) the minimum frequency that is reliably detectable increases. Using a linear model for the difference between differential signals in relation to the applied electric field, the amplitudes extracted from the segmented DFT were converted to field strengths. For a 10 kV amplitude at 10 Hz a resulting field difference of 18.481 kV was extracted where in an ideal case 20 kV are expected. However, the difference is attributed to the limited applied field due to the capacitance and lethargy of the supply.

Another goal was to measure differences in the electric field in a time serious to identify points in a measurement where the field is misbehaving. While extracting frequencies and amplitudes is rather easy when using the proper tools, detecting sudden changes which happen over a short period of time is more challenging. Again, the linear model to translate differences in the measured differential signal to field changes as used. It was calibrated using a step-function with 20 kV step-size with a 2 s period between each step. Subsequently the step-size was reduced by a factor of two. Data was acquired using an oscilloscope and the difference in signal was measured using the internal cursors. The value acquired this way was checked by counting pixels and relating that to the oscilloscope's grid and scale. A signal difference of 99 mV was measured which compares well with the expected value of 100 mV. As a step of 10 kV corresponds to quite high field changes of 0.1 kV/mm it was further decreased. However, at step-sizes of 2 kV and below the difference in signals was barely visible, blending into the signal's noise. Assessing thresholds for the performance to detect field changes was complicated by the high temperature gradient as the ventilation system had to be shut off to vastly improve the signal-to-noise ratio. This least detectable step compiles into about  $10^{-2}$  of 180 kV at 12 cm where a value of  $10^{-4}$  was envisioned.

Working towards the perspective of a feedback-operation of the actual high-voltage supply, the device was put into preliminary operation for test purposes. The output voltage can be set by either the front-panel rotating knobs or the external connectors on the back-panel. It is worthwhile to mention that the range of 0 to 10 on the front-knob corresponds to  $-200$  kV to 200 kV. The output voltage was analyzed using an oscilloscope, first at small voltages of about 25 V. The signal's noise, primarily at 50 Hz, was found to be quite high compared to the signal. Using a voltage divider higher voltages could be probed for while ensuring that the oscilloscope was not damaged. It was found that the noise amplitude at 50 Hz decreases with increasing output voltage and remained approximately constant between 3.44 kV and 5 kV. Thus, it is reasonable to assume that it will either stay at its level when increasing the output voltage further up to 200 kV or decrease. However, a major improvement will be achieved once the supply is set up at its final position and properly connected to a central grounding point (CGP).

This work shows that still several issues regarding the measurement of the electric field using optical methods need to be addressed. The most pressing issue is the stability of the optical setup. This includes both mechanical and thermal stability as the setup is sensitive to vibrations and shocks as well as temperature gradients.

---

Perspectively the setup shall be placed at a location where it is less susceptible to vibrations and air flow originating from the ventilation system.

In case it is found necessary to improve the existing setup before designing a sensor for the TUM-nEDM experiment, redesigning the crystal and electrode holder with an emphasis on stability and simplified adjustability might also be worth investigating. Additionally, identifying crystals that meet the same criteria as quartz, but exhibit higher electro-optic coefficients would help to increase the performance. Likewise, multiple passages of the laser beam through the Pockels crystal would increase the rotation of the plane of polarization, thus increasing the signal measured per electric field unit. With the currently rather tiny crystal (5 mm diameter) this is hardly achievable. Also, in contrast to the longitudinal measurement of the electric field proposed in this work a change towards a transverse measurement could be considered. Then, part of the quartz ring would be replaced with an electro-optic material that is coated for total reflection on the surface facing the center of the ring. The probe laser would enter the material, experience a rotation of its plane of polarization get reflected and leave it again, thus, eliminating the need to drill holes into the electrodes. However, the path length inside the active material would be much shorter as it is constrained by the thickness of the quartz ring which is considerably smaller than its height. The Pockels crystal used for such a setup should have linear electro-optic coefficients that are at least 10 to 100 times as big as in quartz.



---

## Bibliography

- [1] D. N. Spergel, L. Verde, H. V. Peiris, et al. "First-Year Wilkinson Microwave Anisotropy Probe ( WMAP ) Observations: Determination of Cosmological Parameters." In: *The Astrophysical Journal Supplement Series* 148.1 (Sept. 2003), pp. 175–194. DOI: 10.1086/377226 (cit. on p. 1).
- [2] Dennis V Perepelitsa. "Sakharov Conditions for Baryogenesis." In: *Interactions* (2008), pp. 1–3 (cit. on p. 1).
- [3] *The Nobel Prize in Physics 1957* (cit. on p. 1).
- [4] Andrei D Sakharov. "Violation of CP in variance, C asymmetry, and baryon asymmetry of the universe." In: *Pis'ma Zh. Eksp. Teor. Fiz.* 5 (1967), pp. 32–35. DOI: 10.1070/PU1991v034n05ABEH002497 (cit. on p. 1).
- [5] Gary Steigman. "Observational Tests of Antimatter Cosmologies." In: *Annual Review of Astronomy and Astrophysics* 14.1 (Sept. 1976), pp. 339–372. DOI: 10.1146/annurev.aa.14.090176.002011 (cit. on p. 1).
- [6] D. F. Jackson Kimball, S. K. Lamoreaux, and T. E. Chupp. "Tests of fundamental physics with optical magnetometers." In: *Optical Magnetometry*. Ed. by Dmitry Budker and Derek F. Jackson Kimball. 1st ed. Cambridge: Cambridge University Press, 2013. Chap. 18 (cit. on p. 1).
- [7] P. Fierlinger. *Private Communication*. 2015 (cit. on pp. 1–3).
- [8] M. J. Ramsey-Musolf and S. Su. "Low Energy Precision Test of Supersymmetry." In: (2006). DOI: 10.1016/j.physrep.2007.10.001 (cit. on p. 2).
- [9] C. A. Baker, D. D. Doyle, P. Geltenbort, et al. "An Improved Experimental Limit on the Electric Dipole Moment of the Neutron." In: (2007), pp. 1–5. DOI: 10.1103/PhysRevLett.98.149102 (cit. on p. 2).
- [10] Norman F. Ramsey. "Resonance transitions induced by perturbations at two or more different frequencies." In: *Physical Review* 100.4 (1955), pp. 1191–1194. DOI: 10.1103/PhysRev.100.1191 (cit. on pp. 2, 5, 7).
- [11] I. Altarev, D. H. Beck, S. Chesnevskaya, et al. "A next generation measurement of the electric dipole moment of the neutron at the FRM II." In: *Nuovo Cimento della Societa Italiana di Fisica C*. Vol. 35. 4. 2012, pp. 122–127. DOI: 10.1393/ncc/i2012-11271-0 (cit. on pp. 2, 3, 5, 6, 8, 44).
- [12] I. Altarev, M. Bales, D. H. Beck, et al. "A large-scale magnetic shield with 106 damping at millihertz frequencies." In: *Journal of Applied Physics* 117.18 (May 2015), p. 183903. DOI: 10.1063/1.4919366 (cit. on p. 3).
- [13] Michael Sturm. *Measurements and characterization of a laser-based Cs-atomic magnetometer*. 2013 (cit. on pp. 3, 15, 17, 19, VIII).
- [14] J. Pendlebury, W. Heil, Yu. Sobolev, et al. "Geometric-phase-induced false electric dipole moment signals for particles in traps." In: *Physical Review A* 70.3 (Sept. 2004), p. 032102. DOI: 10.1103/PhysRevA.70.032102 (cit. on pp. 5, 7).

## Bibliography

---

- [15] R. Golub, D Richardson, and S.K Lamoreaux. "Measurement of the neutron electric dipole moment using UCN." In: *Ultra-Cold Neutrons*. CRC press, 1991 (cit. on p. 5).
- [16] Bahaa E. A. Saleh and Malvin Carl Teich. *Grundlagen der Photonik*. 2nd ed. Berlin: Wiley-VCH, 2008 (cit. on p. 9).
- [17] Carsten Winnewisser. "Elektrooptische Detektion von ultrakurzen elektromagnetischen Pulsen." PhD thesis. Albert-Ludwigs-Universität Freiburg i. Brsg, 1999 (cit. on p. 9).
- [18] Marvin Weber. *Handbook of Optical Materials*. Vol. 19. Laser & Optical Science & Technology. CRC Press, Sept. 2002. doi: 10.1201/9781420050196 (cit. on p. 10).
- [19] Gorachand Ghosh. "Dispersion-equation coefficients for the refractive index and birefringence of calcite and quartz crystals." In: *Optics Communications* 163.1-3 (May 1999), pp. 95–102. doi: 10.1016/S0030-4018(99)00091-7 (cit. on p. 11).
- [20] Eugene Hecht. *Optics*. 4th ed. Addison-Wesley, 2001 (cit. on pp. 11, 12).
- [21] J. Seufert, M. Fischer, M. Legge, et al. "DFB laser diodes in the wavelength range from 760 nm to 2.5 μm." In: *Spectrochimica Acta - Part A: Molecular and Biomolecular Spectroscopy*. Vol. 60. 14. 2004, pp. 3243–3247. doi: 10.1016/j.saa.2003.11.043 (cit. on pp. 16, 21).
- [22] Hamamatsu. *Si PIN photodiode S3072* (cit. on pp. 17, 44).
- [23] Stanford Research Systems. *SRS Lock-in Amplifier - SR830*. 2002 (cit. on pp. 18, 35, 36).
- [24] K L Corwin, Z T Lu, C F Hand, et al. "Frequency-stabilized diode laser with the Zeeman shift in an atomic vapor." In: *Applied optics* 37.15 (1998), pp. 3295–3298. doi: 10.1364/AO.37.003295 (cit. on pp. 21, 23).
- [25] Valeriy V. Yashchuk, Dmitry Budker, and John R. Davis. "Laser frequency stabilization using linear magneto-optics." In: *Review of Scientific Instruments* 71.2 (2000), p. 341. doi: 10.1063/1.1150205 (cit. on pp. 21, 22).
- [26] Daniel A. Steck. *Cesium D Line Data*. [available online at <http://steck.us/alkalidata> (revision 2.1.4, 23 December 2010)], 2010 (cit. on pp. 22, 29).
- [27] Michael Sturm. *Private Communication*. 2015 (cit. on pp. 24, 28).
- [28] Stanford Research Systems. *SRS Laser Diode Controllers - LDC500 Series*. 2011 (cit. on p. 25).
- [29] Stanford Research Systems. *SRS Analog PID Controller - SIM960*. 2013 (cit. on pp. 25, XIX).
- [30] eagleyard Photonics. *EYP-DFB-0852-00150-1500-TOC03-000x*. 2014 (cit. on p. 28).
- [31] G Heinzel, A Rüdiger, and R Schilling. "Spectrum and spectral density estimation by the Discrete Fourier transform (DFT), including a comprehensive list of window functions and some new flat-top windows." In: (2002), pp. 1–84 (cit. on p. 33).

- [32] Inc. Trek. *Trek Model 610C* (cit. on p. 40).
- [33] J. D. Jackson. "Klassische Elektrodynamik." In: *Walter de Gruyter Berlin New York dritte Auflage 2* (2002), p. 938. DOI: 10.1515/9783110200034.fm (cit. on p. III).



---

## List of Figures

2.1.	Sketch of quartz crystal with alignment of optical axis, laser beam and electric field. . . . .	10
3.1.	Sketch of the optical setup and beam path. . . . .	16
3.2.	Polarimeter board noise for different voltage sources. . . . .	19
3.3.	Discharge curve for both polarities (+ : red, – : blue) . . . . .	20
3.4.	Differential signal of polarimeter board showing the encountered drift . . . . .	21
3.5.	Level scheme for $F = 1 \rightarrow F' = 0$ transition used for the DAVLL. . . . .	22
3.6.	Qualitative illustration of the the magnetic field influence on the absorption resonances and differential signal . . . . .	23
3.7.	SolidWorks® sketch of DAVLL optical setup. . . . .	24
3.8.	Cesium fluorescence from $F = 3 \rightarrow F'$ transition and differential DAVLL curve . . . . .	26
3.9.	PID parameter scan for $P$ and $I$ showing $\log_{10}\langle\varepsilon\rangle$ and $\log_{10}\sigma_\varepsilon$ . . . . .	27
3.10.	Wiring diagram for DAVLL heat stabilization. . . . .	28
3.11.	Electric field simulation for electrodes and crystal. . . . .	30
3.12.	Rendered image of final high voltage assembly. . . . .	31
4.1.	Segmented discrete Fourier transform of a generated 30 Hz signal. . . . .	35
4.2.	Software lock-in scan of a generated 30 Hz signal. . . . .	36
5.1.	Differential signal for high voltage change of 0 kV to 10 kV. . . . .	39
5.2.	Spectral background in the frequency domain for running and switched off ventilation system. . . . .	41
5.3.	Frequency spectra for modulating the high voltage with different frequencies and amplitudes. . . . .	42
5.4.	Measured high voltage modulation amplitudes for 5 kV and 10 kV. . . . .	43
5.5.	Acquired differential signal (time series) with 0.5 Hz step function, step size 10 kV. . . . .	45
A.1.	Maximum amplitude for the magnetic field from a current on the high-voltage electrode. . . . .	V
B.1.	Sketch of laser protection circuit. . . . .	VII
B.2.	Layout for a polarimeter board in normal configuration [13]. . . . .	VIII
B.3.	PID parameter scan for $P$ and $I$ showing $\log_{10}\langle\varepsilon\rangle$ and $\log_{10}\sigma_\varepsilon$ . . . . .	IX
B.4.	Temperature measured by the DAVLL heating sensors over a course of several hours. . . . .	IX
B.5.	SolidWorks® sketch of manufactured electrodes. . . . .	X
B.6.	SolidWorks® sketch of 3D printed crystal holder. . . . .	X
B.7.	Snippet of electric field simulation for electrodes and crystal. . . . .	XI

---

List of Figures

B.8. Verification that no signal is received when no high voltage is passed to the electrodes. . . . .	XI
B.9. Photograph of the final setup (front view). . . . .	XII
B.10. Photograph of the assembled DAVLL without heat stabilization. . . . .	XII
B.11. Photograph of the final setup including the new table with storage space.	XIII
B.12. Changes in differential signal due to changes in high voltage (initial configuration). . . . .	XIV
B.13. Frequency spectrum acquired without laser with ambient light on/off. . . . .	XV
B.14. Frequency spectrum acquired from the DAVLL output. . . . .	XV
B.15. Measured high voltage modulation amplitudes for 5 kV and 10 kV. . . . .	XVI

---

## List of Tables

3.1. Lock-in parameters for the polarimeter board's noise measurements. . .	18
C.1. Files and contents of the shared C++ library. In case of both header and source files present, the functions and classes are exported into the library. Template classes and functions get completely imported with their header files. . . . .	XVII
C.2. List of important optical components in addition to post assemblies and cage system parts. . . . .	XVII
C.3. Adapter-cable pin assignment to connect the laser diode (LD)'s TOC-9 socket to the LDC501. . . . .	XIX
C.4. Cabling for the SRS SIM960 for DB-15/F and DB-9/F for connection to a serial port. . . . .	XIX
C.5. Data format for waveforms recorded with RecordWaveformBIN.py. . .	XX
C.6. Data format for segmented discrete fourier transform (DFT) output files.	XX
C.6. Data format for segmented discrete fourier transform (DFT) output files.	XXI
C.7. Data format for software lock-in output files. . . . .	XXI



# **Appendix**



## APPENDIX A

---

### Derivations of formulas

#### A.1. Time-dependent magnetic field

From the retarded solution for the electro-magnetic wave equations one can derive for the magnetic field

$$\vec{B}(\vec{x}, t) = \frac{\mu_0}{4\pi} \int d^3x' \frac{1}{R} [\vec{\nabla} \times \vec{j}]_{\text{ret}} .$$

Rewriting the integrand to extract the spatial partial derivatives yields

$$[\vec{\nabla} \times \vec{j}]_{\text{ret}} = \vec{\nabla} \times \vec{j}_{\text{ret}} + \frac{1}{c} \frac{\partial \vec{j}_{\text{ret}}}{\partial t'} \times \hat{R} ,$$

which can be used to give the magnetic field in the following form

$$\vec{B}(\vec{x}, t) = \frac{\mu_0}{4\pi} \int d^3x' \left\{ \vec{j}_{\text{ret}}(\vec{x}', t') \times \frac{\hat{R}}{R^2} + \frac{1}{c} \frac{\partial \vec{j}_{\text{ret}}(\vec{x}', t')}{\partial t'} \times \frac{\hat{R}}{R} \right\} . \quad (\text{A.1})$$

Here,  $\vec{R} = \vec{x} - \vec{x}'$ ,  $R = |\vec{R}|$  and  $t' = t - |\vec{x} - \vec{x}'|/c$ . Formulas up to here are taken from Jackson's famous book on classical electrodynamics [33].

To calculate the influence of a current flowing on the high-voltage electrode into the center some assumptions have to be made. First, it is assumed that the length on which the current is flowing is the average distance to the center, which is  $\bar{x} = \frac{d}{3}$ , with the electrode's diameter  $d$ . Second, the current density  $\vec{j}(\vec{x}, t)$  can be decomposed into a stationary, time-dependent and direction-dependent part with  $j_0$ ,  $j_t$  and  $j_{\vec{x}} \equiv \hat{x}$  respectively. For  $j_t$  and  $j_0$  the following is appropriate

$$j_t = \sin(\omega_j t + \phi_j) \\ j_0(\vec{x}) = I_0 \Theta(\bar{x} - x) \delta(y) \delta(z) ,$$

where  $I$  is the current flowing from  $(\bar{x}, 0, 0)$  to  $(x, y, z) = \vec{0}$ . Finally, it is assumed that  $R/c \ll 1$  s since we care about the effect of magnetic fields near the electrode's surface, which makes  $R$  to be on the order of 1 cm. This is equivalent with a retardation  $t' - t$  of approximately 30 ps, which is more than seven orders of magnitude less than the time an UCN needs to travel 1 cm assuming  $v_{\text{UCN}} = 10 \text{ m s}^{-1}$ .  $t'$  is thus replaced with  $t$ .

The integrand in (A.1) is nonzero only for directions of  $\vec{x}'$  that are parallel to the direction of the current density, which is  $\hat{x}$ . This is due to the fact that the origin of

the coordinate system is chosen to be the point where the current flows to and due to the restrictions imposed by the  $\delta$ -functions in  $j_0$ . Thus, the terms of the integrand become

$$\vec{j} \times \frac{\hat{R}}{R^2} = \frac{j_0 j_t}{R^3} \hat{x} \times [(x - x') \hat{x} + y \hat{y} + z \hat{z}] = \frac{j_0 j_t}{[(x - x')^2 + y^2 + z^2]^{3/2}} (y \hat{z} - z \hat{y})$$

$$\frac{1}{c} \frac{\partial \vec{j}}{\partial t} \times \frac{\hat{R}}{R} = \frac{j_0}{c R^2} \frac{\partial j_t}{\partial t} \hat{x} \times \vec{R} = \frac{j_0 / c}{(x - x')^2 + y^2 + z^2} \frac{\partial j_t}{\partial t} (y \hat{z} - z \hat{y}) .$$

Inserted into (A.1) and defining  $r := \sqrt{y^2 + z^2}$  this yields

$$\begin{aligned} \vec{B}(\vec{x}, t) &= \frac{\mu_0 I}{4\pi} \int \int \int dx' dy' dz' \Theta(\bar{x} - x') \delta(y') \delta(z') \left\{ \frac{j_t}{R^{3/2}} + \frac{1}{c R^2} \frac{\partial j_t}{\partial t} \right\} (y \hat{z} - z \hat{y}) \\ &= \frac{\mu_0 I}{4\pi} \int_0^{\bar{x}} dx' \left\{ \frac{j_t}{R^{3/2}} + \frac{1}{c R^2} \frac{\partial j_t}{\partial t} \right\} (y \hat{z} - z \hat{y}) \\ &= \frac{\mu_0 I}{4\pi} \left\{ -j_t \frac{x - x'}{r^2 \sqrt{(x - x')^2 + r^2}} \Big|_0^{\bar{x}} - \frac{1}{c} \frac{\partial j_t}{\partial t} \frac{\arctan\left(\frac{x - x'}{r}\right)}{r} \Big|_0^{\bar{x}} \right\} (y \hat{z} - z \hat{y}) . \end{aligned}$$

The difference in the arctangent is approaching  $-\pi$  for  $r \rightarrow 0$ . In addition, with  $\partial_t j_t \propto \omega_j$ ,  $\mathcal{O}(\omega_j) \lesssim 100$  Hz and the division by  $c$ , the second term is several orders of magnitude smaller than the other. Neglecting this term, the magnetic field becomes

$$\vec{B}(\vec{x}, t) = \frac{\mu_0 I}{4\pi} \sin(\omega_j t + \phi_j) \frac{y \hat{z} - z \hat{y}}{r^2} \left[ \frac{x}{\sqrt{x^2 + r^2}} - \frac{x - \bar{x}}{\sqrt{(x - \bar{x})^2 + r^2}} \right], \quad (\text{A.2})$$

for the magnetic field. This is a rotating field in y-direction, which is defined by the arbitrarily chosen coordinate system and direction of the current. It rotates with frequency  $\omega_j$ . The maximum field amplitude is shown in figure A.1 with  $\vec{x} = (x, 0, z)$  for three constant values of  $z$ .

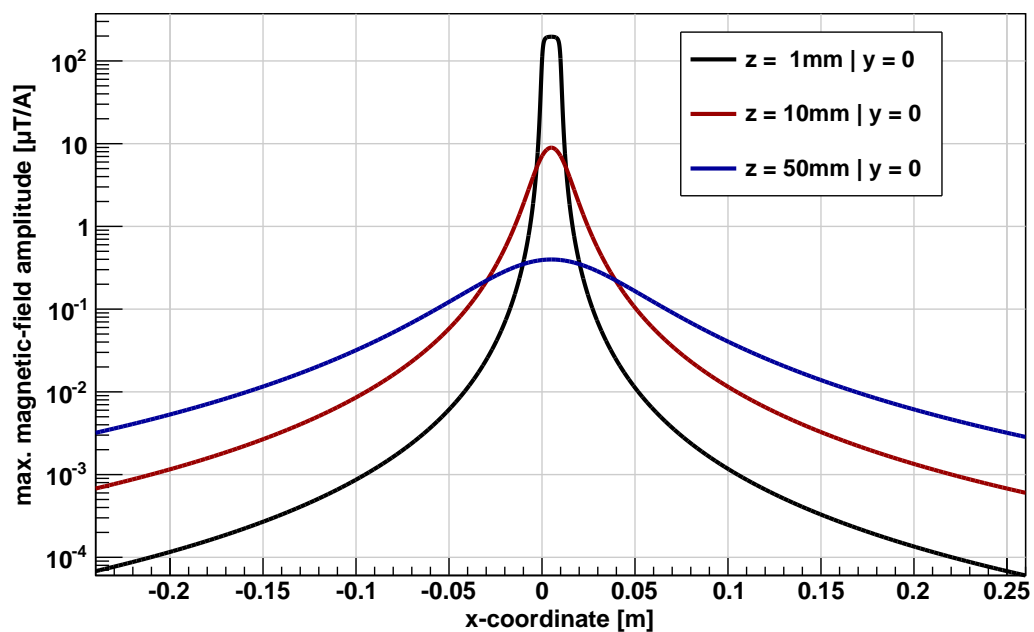


**Figure A.1.:** Maximum amplitude ( $j_0$ ) for the magnetic field due to a current flowing 10 cm radially into the center of the electrode ( $x = 0$ ). The field is shown for three distances from the current.

## A.2. Larmor precession adjustment for disturbances of an uniaxial field

The movement of a magnetic moment  $\vec{\mu}$  in a magnetic field is described by  $\vec{\tau} = \vec{\mu} \times \vec{B}$  with the torque  $\vec{\tau} = d\vec{L}/dt$ . Here  $\vec{L} = -\vec{\mu}/\gamma$  is the angular momentum. This yields the system of differential equations

$$\frac{d\vec{\mu}}{dt} = -\gamma \vec{\mu} \times \vec{B}.$$

For an uniform magnetic field oriented for example in z-direction, the solution is rather simple, yielding

$$\vec{\mu}(t) = \mu \begin{pmatrix} \cos [\omega_L t + \phi] \sin \vartheta \\ \sin [\omega_L t + \phi] \sin \vartheta \\ \cos \vartheta \end{pmatrix},$$

where the parameters  $\phi$  and  $\vartheta$  are defined by the initial conditions at  $t = 0$ . The frequency with which the magnetic moment precesses around the z-axis is the Larmor frequency  $\omega_L = \gamma B_z$ .

If a field  $B_x \hat{e}_x$  is added, the system of differential equations becomes

$$\frac{d\vec{\mu}}{dt} = -\gamma \begin{pmatrix} 0 & B_z & 0 \\ -B_z & 0 & B_x \\ 0 & -B_x & 0 \end{pmatrix} \cdot \vec{\mu}.$$

First, let  $B_x$  be stationary and choose the initial conditions to  $\vec{\mu}(t = 0) = \mu \hat{e}_x$ . Using Mathematica® and manual simplification of its output, this yields

$$\vec{\mu}(t) = \mu \frac{1}{1 + \alpha^2} \begin{pmatrix} \alpha^2 + \cos [\omega_L \sqrt{1 + \alpha^2} t] \\ \sqrt{1 + \alpha^2} \sin [\omega_L \sqrt{1 + \alpha^2} t] \\ \alpha - \alpha \cos [\omega_L \sqrt{1 + \alpha^2} t] \end{pmatrix},$$

with  $\alpha = \frac{\omega_x}{\omega_L}$ . A quick test for  $|\vec{\mu}| \stackrel{!}{=} \mu$  confirms this solution. The z-component can alternatively be written as

$$\mu_z(t) = 2\alpha \sin^2 \left( \frac{\omega_L \sqrt{1 + \alpha^2}}{2} t \right).$$

The conclusion from this result is first that the original Larmor frequency given by  $\gamma B_z$  is altered by a factor of  $\sqrt{1 + \omega_x^2/\omega_L^2}$ , which can introduce errors. Second, the z-component is not stationary anymore as it now oscillates around zero with half of the altered Larmor frequency.

## APPENDIX B

---

### Additional figures

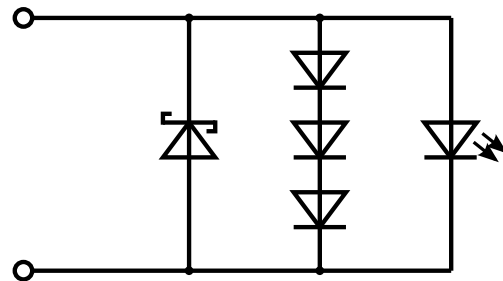


**Figure B.1:** Sketch of laser protection circuit with one laser diode parallel to a series of diodes parallel to a Schottky diode.

## Appendix B. Additional figures

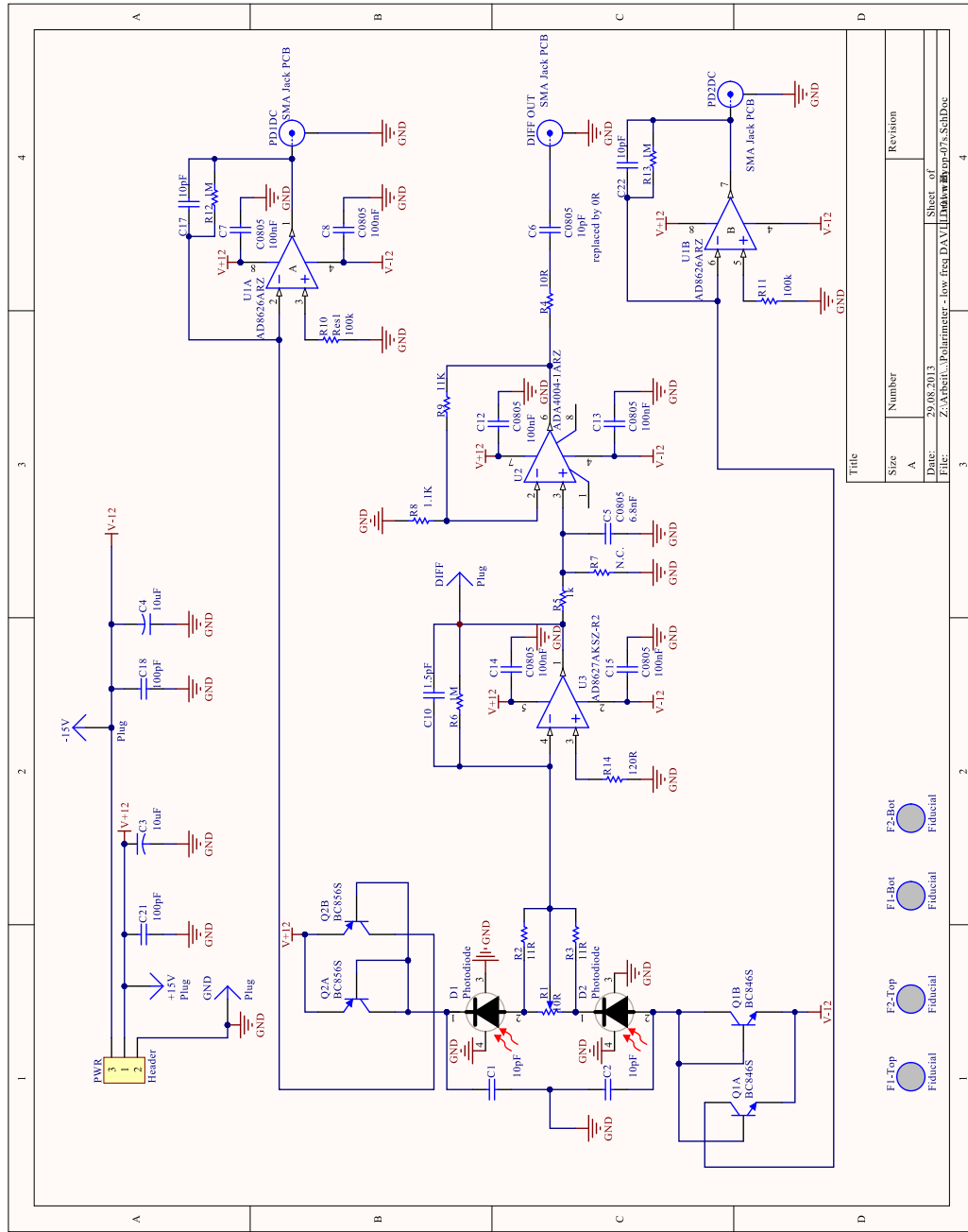


**Figure B.2.:** Layout for a polarimeter board with two single-sided and one differential path, each with its own (set of) amplifiers. The parts listed here form the normal configuration [13].

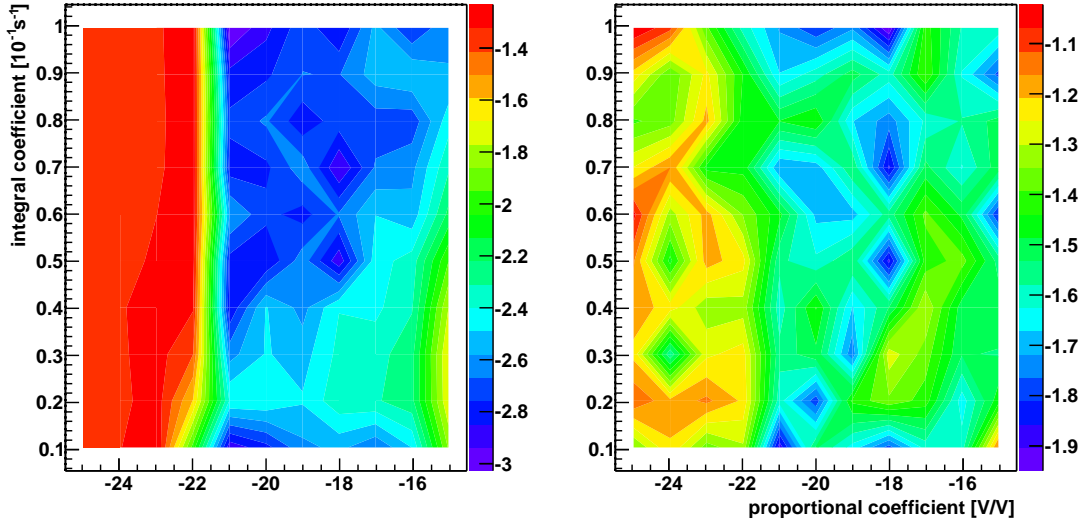


**Figure B.3:** PID parameter scan for *proportional* and *integral* control paths for  $0.01 \leq [I] \leq 0.1$ . The color scale is logarithmic, with  $\log_{10}\langle\epsilon\rangle$  and  $\log_{10}\sigma_\epsilon$  on the left and right side respectively. Violet and blue colors represent small and desirable values whereas green and red correspond to parameter pairs that lead to offsets and/or fluctuations.

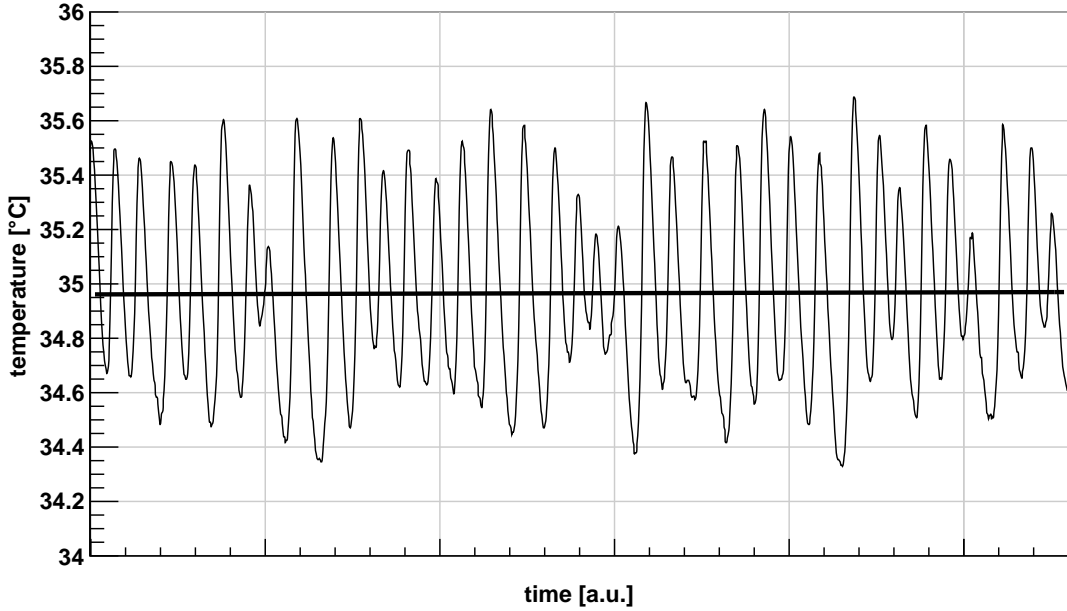


**Figure B.4:** Temperature measured at the optical DAVLL assembly. Small oscillations  $< 0.6^\circ\text{C}$  around the setpoint of  $35^\circ\text{C}$  appear on the order of seconds due to the lethargy of heat loss and the heating process. Apart from those there is no long-term drift measurable.

## Appendix B. Additional figures

---

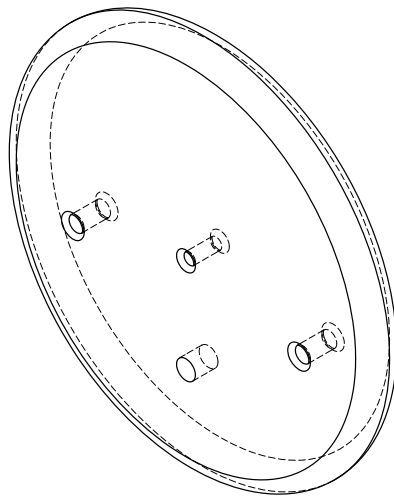


**Figure B.5.:** SolidWorks® sketch of the electrodes manufactured for high-voltage operation. It features a 3 mm hole for the laser to pass through, two 4 mm assembly holes and a M6 thread hole for cable attachment.

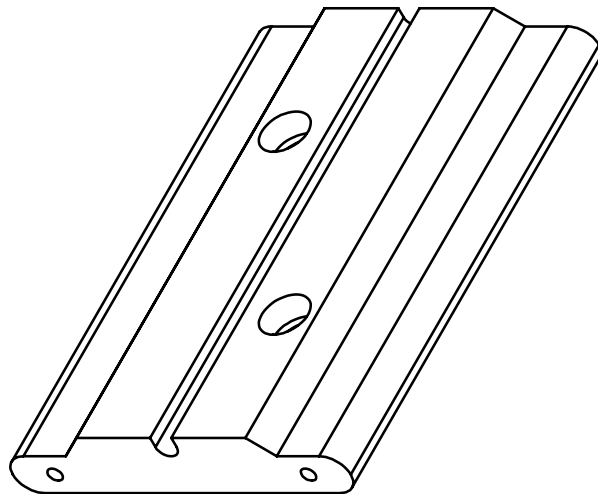


**Figure B.6.:** SolidWorks® sketch of the crystal holder 3D printed from ABS plastic. It has two holes for countersunk bolts and two M4 thread holes on each end for electrode attachment.

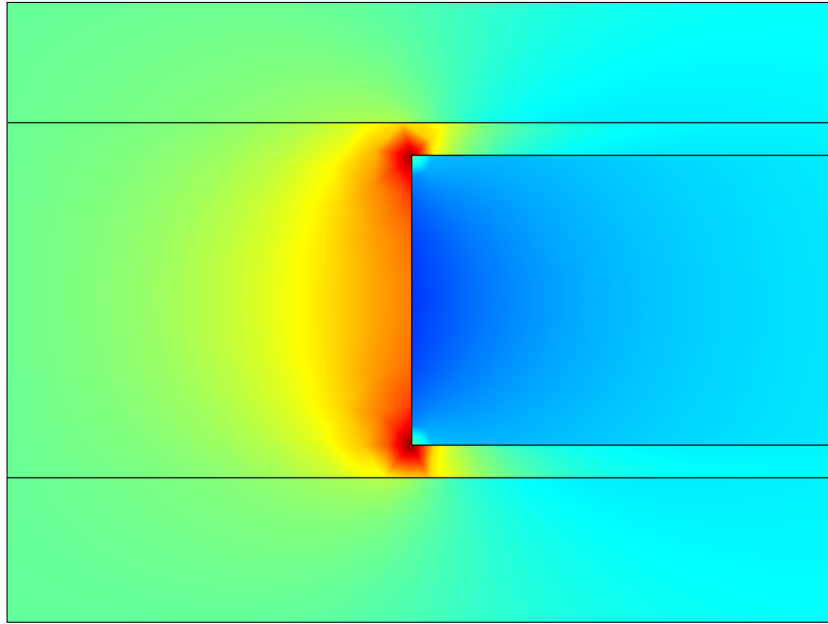


**Figure B.7.:** Snippet of electric field simulation using COMSOL® showing the crystal's left end inside the holder. The maximum field on the crystal's sharp edges is on the order of  $2 \text{ kV mm}^{-1}$ . The color range extends from  $0 \text{ kV mm}^{-1}$  to just over  $2 \text{ kV mm}^{-1}$ .

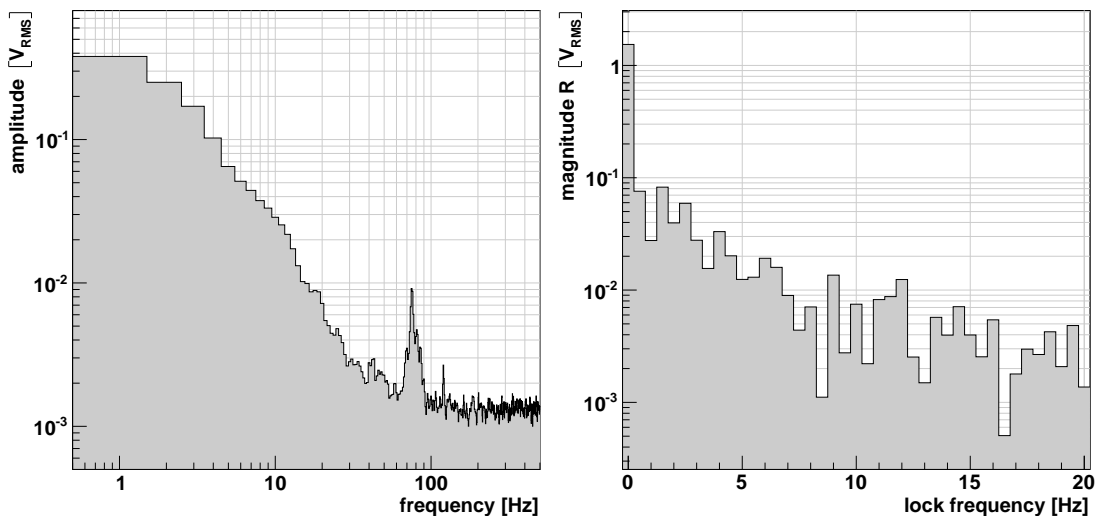


**Figure B.8.:** Verification that no signal is received from the function generator ( $10 \text{ V}_{\text{pp}}$  at  $10 \text{ Hz}$ ) when no high voltage is passed on to the electrodes. The left shows the segmented DFT result as a linear spectrum while the right show the results using the software lock-in algorithm.

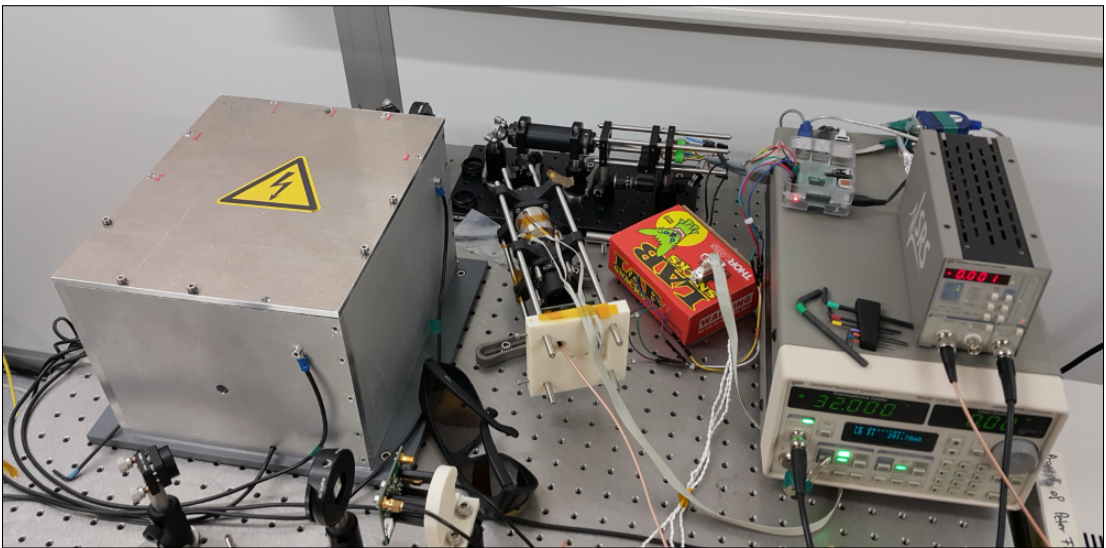


**Figure B.9.:** Photograph of the final setup seen from the front. The beam path starts in the background towards the left, enters the high-voltage box and ends at the polarimeter board in the front.

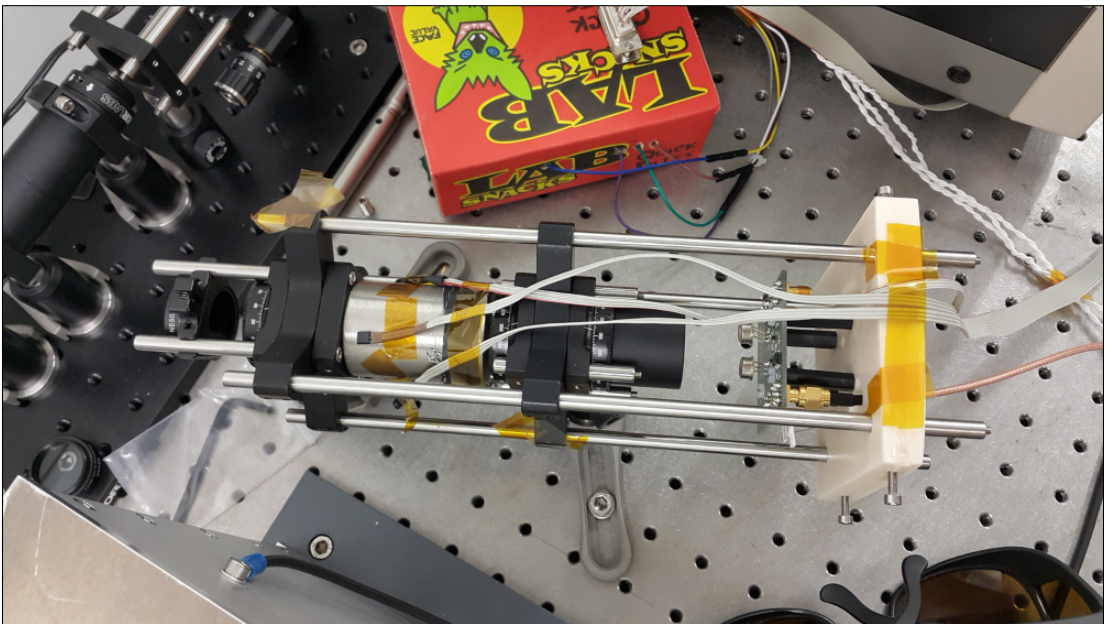


**Figure B.10.:** Photograph of the assembled DAVLL without heat stabilization. The beam enters from the left hand side.

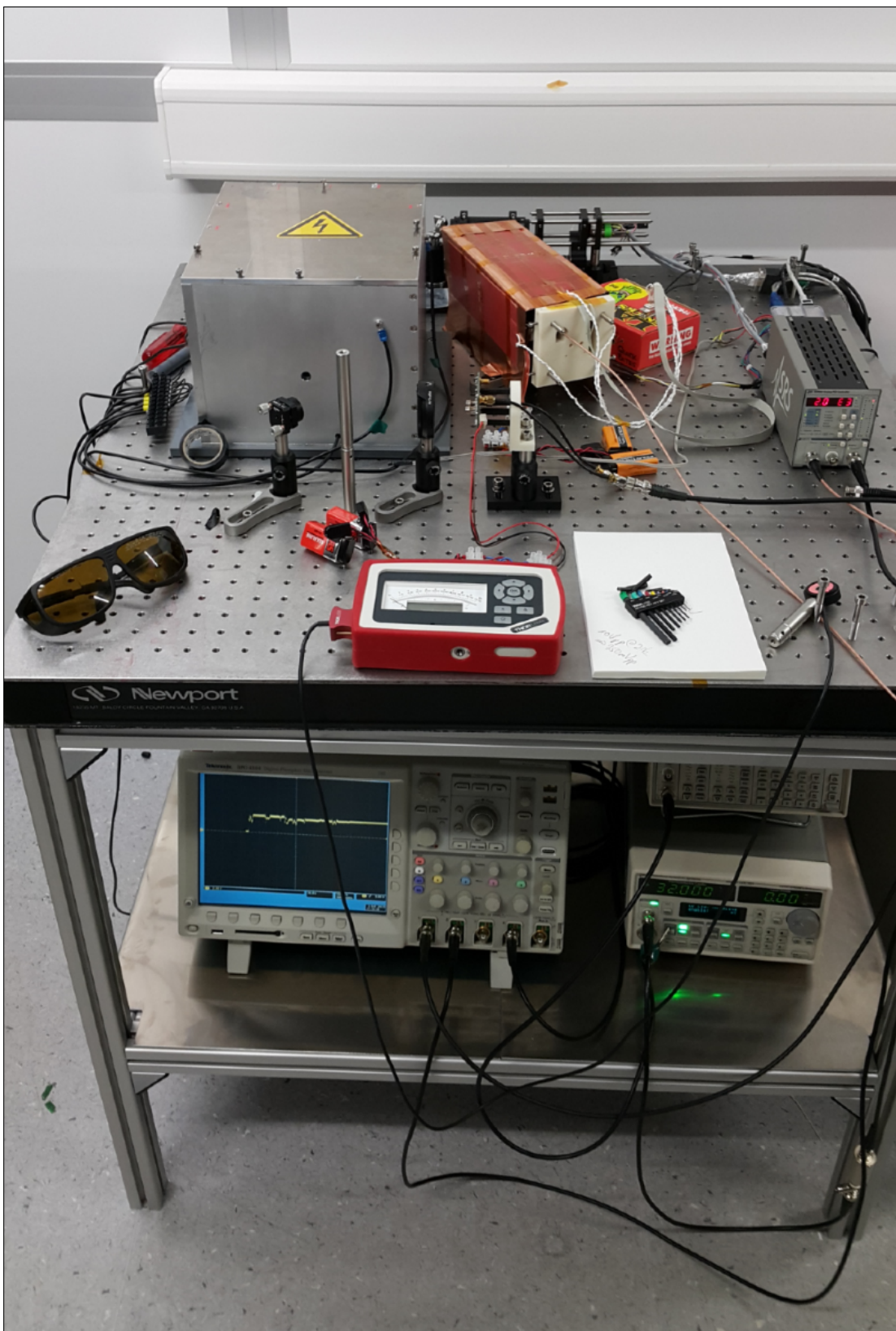


**Figure B.11.:** Photograph of the final setup including the new table with storage space.

## Appendix B. Additional figures

---

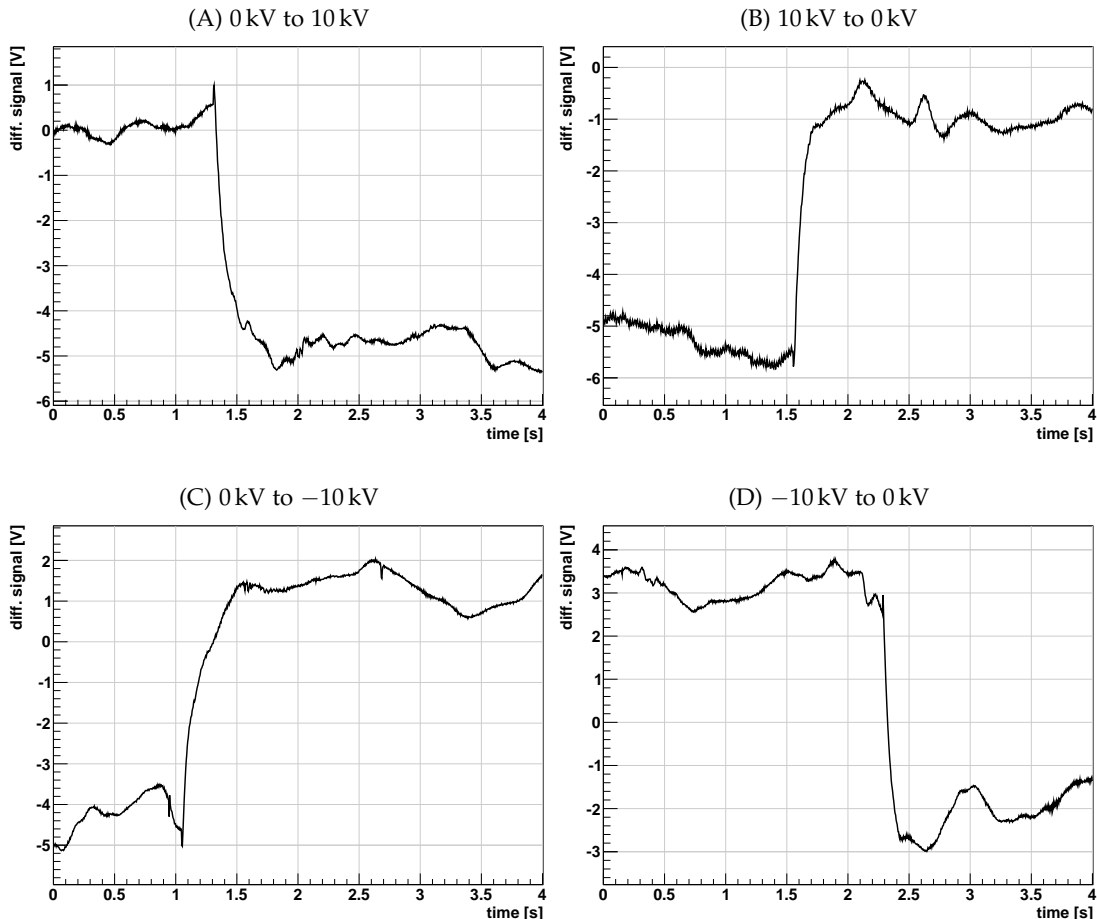


**Figure B.12.:** Change in differential signal due to changes in high voltage. Measurements A through D were taken with the initial setup before realignment and installation of a DAVLL.

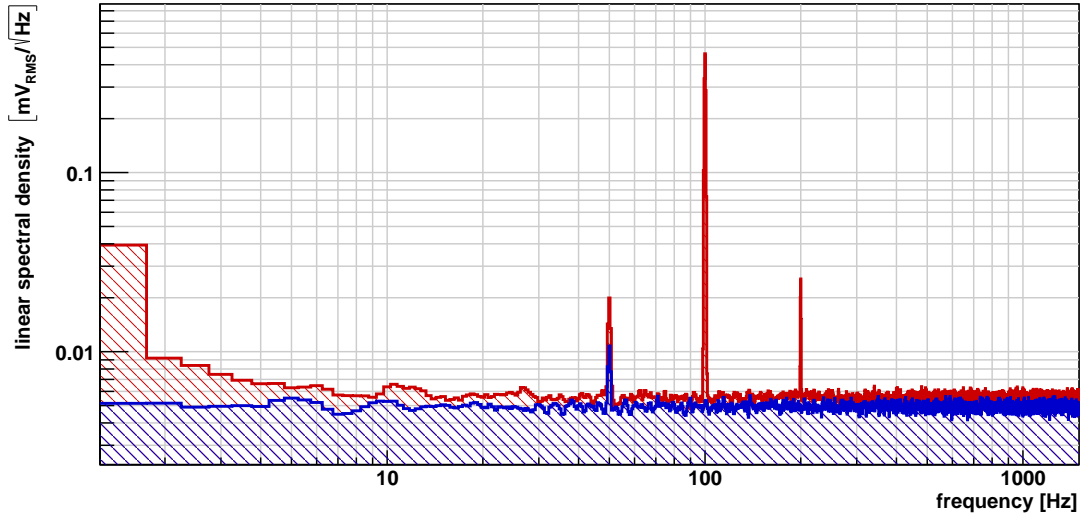


**Figure B.13.:** Frequency spectrum acquired without incident laser light and ambient light switched on (red) and off (blue).

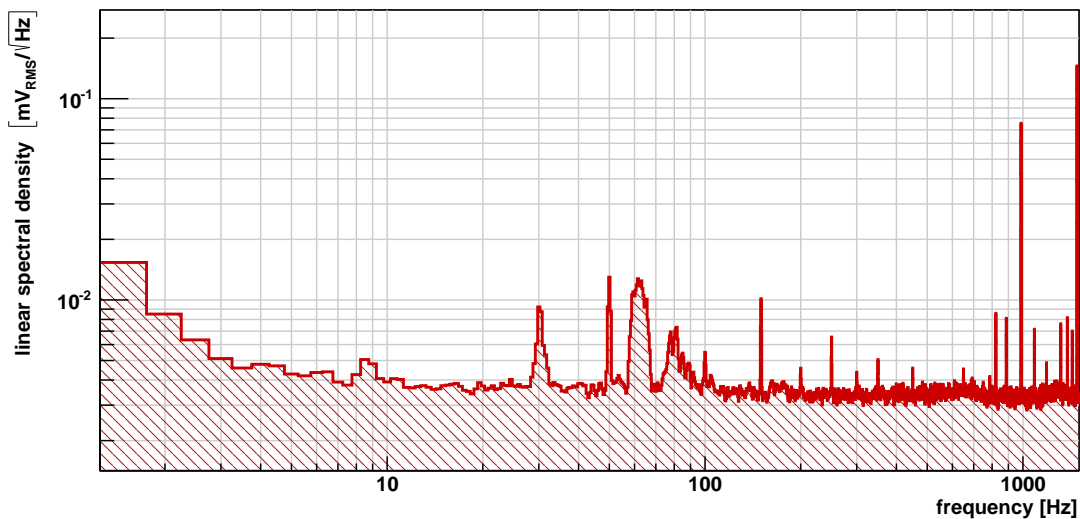


**Figure B.14.:** Frequency spectrum acquired from the dichroic atomic vapor laser lock (DAVLL) output after the voltage divider.

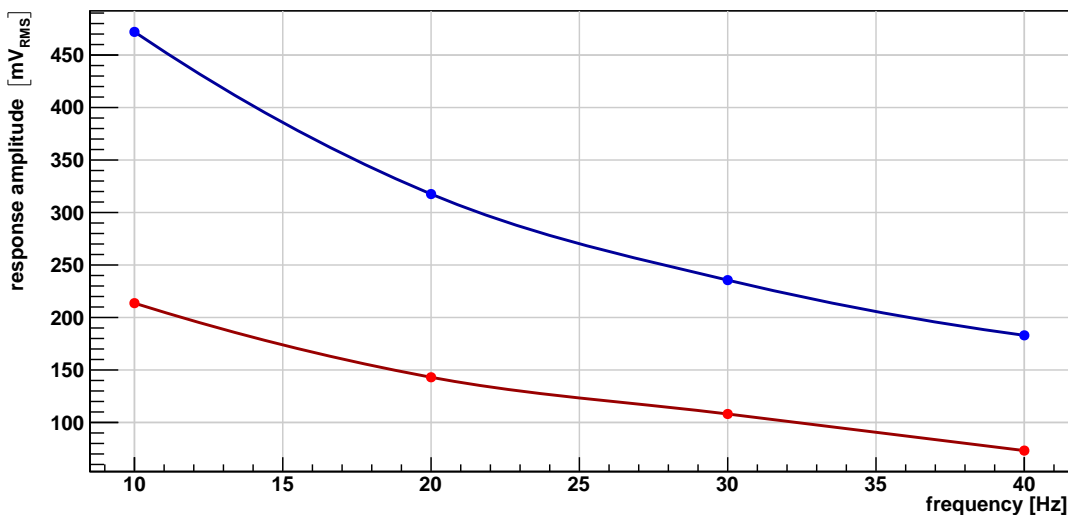


**Figure B.15.:** Measured high voltage modulation amplitudes for 5 kV (red) and 10 kV (blue) setpoints. Both curves are proportional to a decreasing exponential, which is caused by the lethargy of the system, i.e. the non-instantaneous build-up of the high voltage on the electrodes.

## APPENDIX C

---

### Additional tables

**Table C.1.:** Files and contents of the shared C++ library. In case of both header and source files present, the functions and classes are exported into the library. Template classes and functions get completely imported with their header files.

Filename	Description
Algorithm.h	Provides algorithms to reduce data by averaging adjacent values.
Convert.h	Conversion algorithms from and to byte as well as header parsing
CVcommon.(h/cpp)	typedef and memcpy replacements for portability
File.(h/cpp)	Routines for I/O, especially reading and writing binary files
Filters.h	Template class (static members) implementing low-, high-, band-pass and band-stop filters
LockIn.h	Software lock-in class (static member) using double phase-sensitive-detection
MathTools.h	Mathematical functions, e.g. averaging and Python-like logspace
SegmentedFFT.h	Template class for segmented DFT calculation
String.(h/cpp)	Implementing non-C++ methods like ToString(T obj) or Split
Waveform.h	Structs for waveform header information
Windows.h	Template class (static members) for window functions, e.g. Hamming or Nuttall

### C.1. List of optical elements

**Table C.2.:** List of important optical components in addition to post assemblies and cage system parts.

Qty.	Part Number	Description	Vendor
2	BB05-E03	Ø1/2" Broadband Dielectric Mirror, 750 nm to 1100 nm	THORLABS
1	C330TMD-B	$f = 3.1$ mm, NA = 0.68, Mounted geltech Aspheric Lens, AR: 600 nm to 1050 nm	THORLABS
2	CRM1/M	Cage Rotation Mount for Ø1" Optics, SM1-Threaded, M4 Tap	THORLABS
1	IOT-5-850-VLP	Free-Space Tandem Isolator, 850 nm, Ø4.7 mm Max Beam, 1.7 W Max	THORLABS
2	KMS/M	Compact Kinematic Mirror Mount, M4 Taps for Post Mounting	THORLABS

continued on next page

## Appendix C. Additional tables

---

Qty	Part Number	Description	Vendor
2	LCPo2/M	30 mm to 60 mm Cage Plate Adapter, Metric	THORLABS
2	MH12	Mirror Holder for $\varnothing 1/2''$ Optics	THORLABS
1	NE03A	$\varnothing 25$ mm Absorptive ND Filter, SM1-Threaded Mount, Optical Density: 0.3	THORLABS
1	NE10A	$\varnothing 25$ mm Absorptive ND Filter, SM1-Threaded Mount, Optical Density: 1.0	THORLABS
1	NE20A	$\varnothing 25$ mm Absorptive ND Filter, SM1-Threaded Mount, Optical Density: 2.0	THORLABS
1	NE50A	$\varnothing 25$ mm Absorptive ND Filter, SM1-Threaded Mount, Optical Density: 5.0	THORLABS
1	POLARIS-K05	Polaris™ Low Drift $\varnothing 1/2''$ Mirror Mount, 3 Low-profile Hex Adjusters	THORLABS
1	PRM05/M	High-Precision Rotation Mount for $\varnothing 1/2''$ (12.5 mm) Optics, Metric	THORLABS
1	QRC1A	SM1-Threaded Quick-Release Cage Mount for the 30 mm Cage System	THORLABS
3	RSP1/M	Rotation Mount for $\varnothing 25.4$ mm Optics, Metric, One SM1RR Retaining Ring Included	THORLABS
2	WP10-B	Wollaston Prism, 20° Beam separation, 650 nm to 1050 nm AR Coating	THORLABS
2	WPH05M-850	$\varnothing 1/2''$ Mounted Zero-Order Half-Wave-Plate, $\varnothing 1$ in Mount, 850 nm	THORLABS
1	WPQ05M-850	$\varnothing 1/2''$ Mounted Zero-Order Quarter-Wave-Plate, $\varnothing 1$ in Mount, 850 nm	THORLABS

---

## C.2. Cables and wiring

**Table C.3.:** Laser diode and thermoelectric cooling adapter-cable pin assignment for connecting the TOC-9 socket to the SRS LDC<sub>501</sub>.

DB-9/M (TEC)	DB-9/F (LD)	TOC-3	Signal
1,2		1	TE+
3,4		8	TE-
7		2	Sensor+
8		3	Sensor-
	1,2		Interlock (shorted)
	5	4	LD Cathode
	6	7	PD Cathode
	7	6	PD Anode
	9	5	LD Anode, to Schottky pin 2

**Table C.4.:** Cabling for the SRS SIM960 with the DB-15/F and DB-9/F connected to the PID controller and computer RS-232 port, respectively. DB-15/F pins 1, 8 and 9 are connected to form a common ground near the power supplies. The signal names and descriptions are taken from the PID's manual [29].

DB-15/F	DB-9/F	Signal	Description
1	5	SIGNAL_GND	Ground reference for signal
3	7	RTS	HW Handshake (+5 V = talk; GND = stop)
4	8	CTS	HW Handshake (+5 V = talk; GND = stop)
7		-15 V	Power supply (analog circuitry)
8		PS_RTN	Power supply return
9		CHASSIS_GND	Chassis ground
10	3	TxD	Async data (start bit = "1" = +5 V; "0" = GND)
11	2	RxD	Async data (start bit = "1" = +5 V; "0" = GND)
13		+5 V	Power supply (digital circuitry)
14		+15 V	Power supply (analog circuitry)

### C.3. Data and file formats

**Table C.5.:** Data format for waveforms recorded with `RecordWaveformBIN.py`.

Data type	Description
time-stamp	
int32	years since 1900
int32	months since January, [0, 11]
int32	day of the month, [0, 31]
int32	hours after midnight, [0, 23]
int32	minutes after the hour, [0, 59]
int32	seconds after the minute, [0, 59]
data header	
byte8	value type size in byte, e.g. 4 for float32
uint32	$n$ , number of data points
$5 \times$ float32/64	waveform output scaling values
2 × char	waveform x- and y-unit
data values	
$n \times$ float32/64	data points

**Table C.6.:** Data format for segmented discrete fourier transform (DFT) output files.

Data type	Description
data header	
float32/64	sampling frequency
float32/64	frequency resolution (linear spacing)
float32/64	Fourier transform scaling factor $S_1$
float32/64	Fourier transform scaling factor $S_2$
float32/64	normalized equivalent noise bandwith (NENBW)
float32/64	effective noise bandwith (ENBW)
uint32	window type used, see TODO INPUT REFERENCE
data values	
continued on next page	

---

### C.3. Data and file formats

**Table C.6.:** Data format for segmented discrete fourier transform (DFT) output files.

Data type	Description
$n \times \text{float32}/64$	Fourier transform results (histogram values)

**Table C.7.:** Data format for software lock-in output files.

Data type	Description
$\frac{n}{3} \times \text{float32}/64$	frequency values
$\frac{n}{3} \times \text{float32}/64$	averaged R value for each frequency
$\frac{n}{3} \times \text{float32}/64$	phase for each frequency



## Statutory Declaration

I declare that I have authored this thesis independently, that I have not used other than the declared sources/resources, and that I have explicitly marked all material which has been quoted either literally or by content from the used sources.

*Ich erkläre hiermit, dass ich die vorliegende Arbeit selbstständig verfasst, andere als die angegebenen Quellen/Hilfsmittel nicht benutzt, und die den benutzten Quellen wörtlich und inhaltlich entnommene Stellen als solche kenntlich gemacht habe.*

München,

\_\_\_\_\_

\_\_\_\_\_

Date

Signature

